Pulsed Miocene range growth in northeastern Tibet: Insights from Xunhua Basin magnetostratigraphy and provenance

Richard O. Lease[1,†], Douglas W. Burbank[1], Brian Hough[2], Zhicai Wang[3], and Daoyang Yuan[3]

[1]*Department of Earth Science, University of California, Santa Barbara, California 93106, USA*
[2]*Department of Earth and Environmental Sciences, University of Rochester, Rochester, New York 14627, USA*
[3]*State Key Laboratory of Earthquake Dynamics, Institute of Geology, China Earthquake Administration, Beijing 100029, China*

ABSTRACT

Sedimentary rocks in Tibetan Plateau basins archive the spatiotemporal patterns of deformation, erosion, and associated climate change that resulted from Cenozoic continental collision. Despite growing understanding of basin development in northeastern Tibet during initial India-Asia collision, as well as in the late Miocene–Holocene, surprisingly little is known about the intervening period: a time when the plateau may have undergone fundamental tectonic changes. To fill this gap, we present new magnetostratigraphy from a >2300-m-thick fluviolacustrine succession that spans ca. 30–9.3 Ma. An integrated analysis of sedimentology, subsidence, and provenance from this section reveals the sequential, pulsed erosion of multiple ranges bordering the Xunhua Basin. Emergence of the WNW-trending Laji Shan is highlighted by a doubling of sediment accumulation rates between 24 and 21 Ma and a transition to coarse alluvial facies at 20.3 Ma. Detrital zircon U/Pb age spectra show that these coarse sediments came from basement terranes within the Laji Shan. Together these observations suggest accelerated growth of the Laji Shan and its coupled foreland basin at ca. 22 Ma. The most rapid accumulation rates in Xunhua Basin occur within the finest-grained strata and suggest an underfilled basin during the fastest interval of Laji Shan deformation. Growth of the Laji Shan occurred northward of the contemporaneous plateau margin, which had been defined since ca. 45–50 Ma by the West Qinling, lying ~60 km farther south. Hence, following ~20–25 m.y. of apparent stability, the deformation front in this region jumped ~60 km to the north at ca. 22 Ma. Subsequently, growth of the north-trending Jishi Shan occurred at ca. 13 Ma and is highlighted by an acceleration in Xunhua Basin accumulation rates between 12 and 9 Ma, as well as by a significant change in detrital zircon provenance of nearby Linxia Basin deposits by 11.5 Ma. Initial growth of the WNW-trending Laji Shan in the early Miocene and subsequent growth of the north-trending Jishi Shan ~10 m.y. later support interpretations of a middle Miocene kinematic reorganization in northeastern Tibet.

INTRODUCTION

Over the past decade, growing evidence indicates that contractional deformation near the present northern margin of the Tibetan Plateau commenced a few million years after initial India-Asia continental collision (Yin et al., 2002, 2008a; Yin and Harrison, 2000), despite the >3000 km distance separating northeastern Tibet from the plate boundary at ca. 50 Ma (Molnar and Stock, 2009). Along the northeastern plateau margin, a regional 25° clockwise rotation by ca. 41 Ma (Dupont-Nivet et al., 2008) and the onset of localized thrust-induced cooling (Clark et al., 2010) and fault gouge (Duvall et al., 2011) at ca. 45–50 Ma directly support an Eocene onset of contractional tectonism in the Xining-Lanzhou region (Fig. 1A). To the west, along the northern plateau margin, initiation of a suite of contractional structures in the northern Qaidam Basin and adjacent ranges at ca. 65–50 Ma (Yin et al., 2008a) corroborates this early deformation. Furthermore, the oldest strata within continuous Cenozoic stratigraphic successions in both the Xining (Dai et al., 2006) and Qaidam Basins (summarized in Yin et al., 2008b) are nearly coeval with the initial phase of India-Asia continental collision.

On the other hand, several studies document an episode of accelerated deformation, erosion, and deposition initiating in the late Miocene on both the northern and eastern plateau margins. Some of the most compelling evidence derives from low-temperature thermochronological histories in uplifted mountain ranges where age-depth or time-temperature relationships exhibit a clear transition to rapid cooling. Accelerated late Miocene–Pliocene development of the eastern plateau margin is revealed by detailed thermochronological records from the Longmen Shan (Godard et al., 2009), Min Shan (Kirby et al., 2002), and Gonga Shan areas (Clark et al., 2005; Ouimet et al., 2010), as well as fission-track-length modeling from a portion of the Qinling (Enkelmann et al., 2006). In northeastern Tibet, thermochronologic age-elevation relationships also clearly demarcate a late Miocene onset of accelerated cooling in the Liupan Shan (Zheng et al., 2006) and north Qilian Shan (Zheng et al., 2010), which is corroborated by sedimentological and magnetostratigraphic archives adjacent to these ranges (Fig. 1A; Bovet et al., 2009; Wang et al., 2011a). Finally, magnetostratigraphic records adjacent to the Riyue Shan (Fang et al., 2005; Lease et al., 2007), Qinghai Nan Shan (Zhang et al., 2011), and Gonghe Nan Shan (Craddock et al., 2011) reveal the late Miocene emergence of these ranges.

Despite increasing knowledge of plateau-margin deformation during both the Eocene onset of continental collision as well as during the late Miocene, geological knowledge of the interval between these two episodes remains sparse. For example, the large body of work revealing extensive late Miocene–Pliocene range growth in northeastern Tibet (Fig. 1A) stands in contrast to only meager evidence for Oligocene–middle Miocene range growth. Proxy data sets, such as middle Miocene vertical-axis rotations (Yan et al., 2006) or decreases in detrital thermochronology lag times (Zheng et al., 2003), are often unable to delimit proximate causes (Zhang et al., 2011) or source areas. In addition, recent thermochronological results that suggest

---

†Present address: Institut für Geowissenschaft, Universität Tübingen, 72074 Tübingen, Germany; e-mail: richard.lease@uni-tuebingen.de
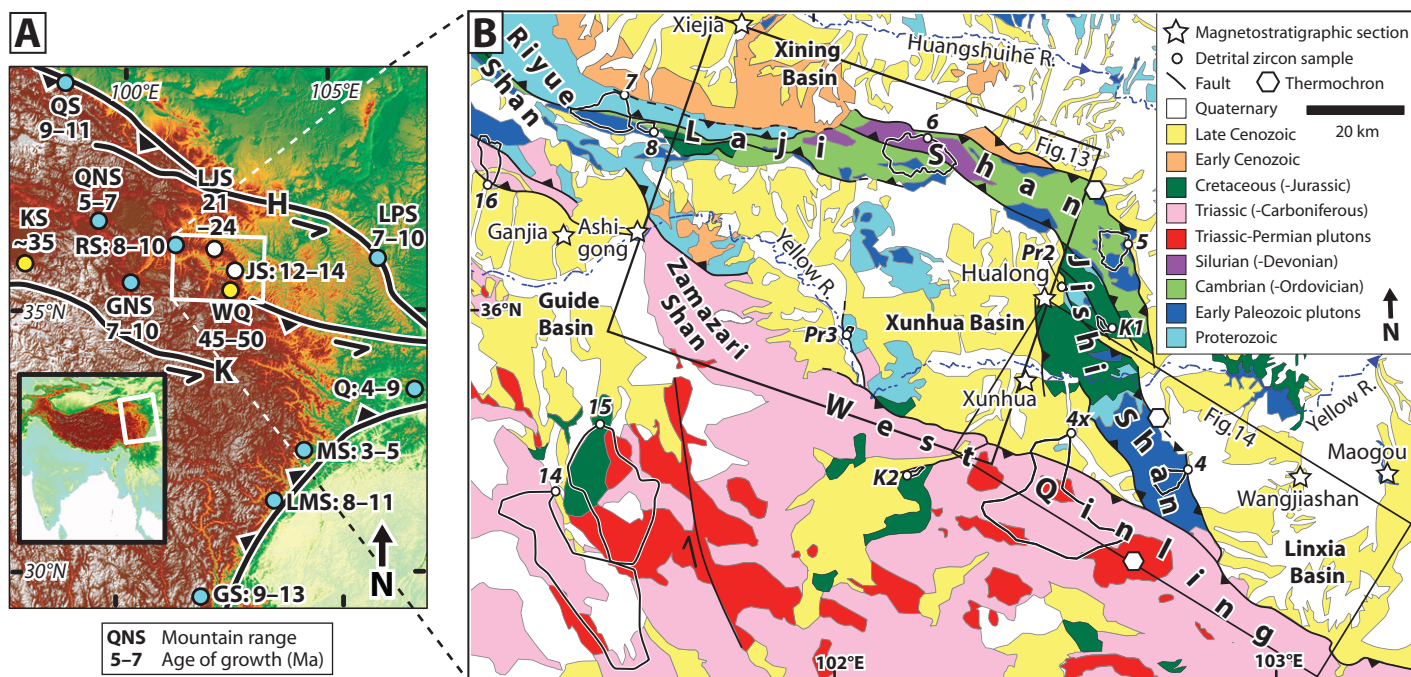
Figure 1. (A) Northeastern margin of the Tibetan Plateau showing ages of onset of accelerated Cenozoic range growth derived from bedrock thermochronology and sedimentary records. Contractional deformation across WNW-trending faults commenced shortly after initial India-Asia continental collision (yellow circles), with a later phase of incremental expansion and accelerated exhumation in the late Miocene (blue circles) occurring toward both the east and north. In this paper, we discuss new evidence for early–middle Miocene range growth (white circles). Data from west to east: the Kunlun Shan (KS) ca. 35 Ma (Clark et al., 2010), Qilian Shan (QS) 9–11 Ma (Bovet et al., 2009; Zheng et al., 2010), Qinghai Nan Shan (QNS) 5–7 Ma (Zhang et al., 2011), Gonghe Nan Shan (GNS) 7–10 Ma (Craddock et al., 2011), Riyue Shan (RS) 8–10 Ma (Fang et al., 2005; Lease et al., 2007), Gonga Shan area (GS) 9–13 Ma (Clark et al., 2005; Ouimet et al., 2010), Laji Shan (LJS) 21–24 Ma and Jishi Shan (JS) 12–14 Ma (Lease et al., 2011; this paper), West Qinling (WQ) 45–50 Ma (Clark et al., 2010; Duvall et al., 2011), Longmen Shan (LMS) 8–11 Ma (Godard et al., 2009), Min Shan (MS) 3–5 Ma (Kirby et al., 2002), Qinling (Q) 4–9 Ma (Enkelmann et al., 2006), and Liupan Shan (LPS) 7–10 Ma (Wang et al., 2011a; Zheng et al., 2006). K—Kunlun fault and H—Haiyuan fault. (B) Geological map of Xunhua Basin study area with magnetostratigraphic section locations (stars) (this paper; Dai et al., 2006; Fang et al., 2003, 2005; Hough et al., 2011), modern detrital zircon samples (numbered circles) (this paper; Lease et al., 2007), and major thermochronology transects (hexagons) (Lease et al., 2011; Clark et al., 2010) shown. Geology is modified after Qinghai Bureau of Geology and Mineral Resources (QBGMR) (1991). For each detrital zircon sample, the associated catchment is outlined.

sequential, early and middle Miocene growth of the Laji-Jishi Shan complex (Lease et al., 2011) have yet to be substantiated by stratigraphic archives from adjacent basins.

In fact, few sedimentary successions from northeastern Tibet provide detailed histories of both erosion and deposition between 40 and 10 Ma. More studies have focused on the widespread Upper Miocene–Pliocene basin fills that display increases in sediment accumulation rates and grain sizes (Fang et al., 2003, 2005; Zhang et al., 2011), new source terranes (Lease et al., 2007), and changes in stable isotopic compositions (Dettman et al., 2003; Hough et al., 2011). Many of these changes occurred ca. 11–8 Ma and have been interpreted to indicate accelerated deformation, basin development, and the emergence of adjacent mountain ranges on the margin of the plateau since this time (e.g., Dayem et al., 2009; Molnar and Stock, 2009).

Factors that remain unknown are whether significant basin development and contractional deformation took place in the Xining-Lanzhou region of northeastern Tibet between 40 and 10 Ma, and if so, whether these processes were isolated or part of a continuum. Several outstanding questions concerning the Oligocene–middle Miocene depositional history of northeastern Tibet remain unanswered: (1) Was accumulation slow and steady for tens of millions of years (e.g., Dai et al., 2006) or was accumulation punctuated by the onset of flexure (e.g., Fang et al., 2003) or sediment ponding (e.g., Métivier et al., 1998) adjacent to newly uplifted ranges? (2) Was sediment derived primarily from distal sources in the plateau interior to the south or from newly exposed sources outboard of the contemporaneous plateau margin? (3) When did a once-contiguous foreland basin become compartmentalized into several smaller intermontane basins?

For clear answers to these questions, we need to define the onset, pace, nature, and extent of basin development and range growth. In this paper, we integrate new magnetostratigraphic, provenance, subsidence, and sedimentological analyses from the northern Xunhua Basin with extant work to assess the late Oligocene-to-Pliocene depositional and tectonic history of northeastern Tibet. We document sequential growth of the Laji-Jishi Shan complex in northeastern Tibet in two discrete phases: punctuated erosion of the Laji Shan at ca. 22 Ma and of the Jishi Shan at ca. 13 Ma.

GEOLOGICAL SETTING

The Tertiary Xunhua Basin (herein simply referred to as Xunhua Basin) is located ~100 km southeast of Xining, Qinghai province, China (Fig. 1B). Xunhua Basin fill occupies a surface

area of ~3300 km^2 with elevations ranging from 1870 m (base level of the Yellow River at the town of Xunhua) to 3000 m. Headward incision by the ancestral Yellow River and its tributaries through this region starting at ca. 1.7 Ma (Craddock et al., 2010; Harkins et al., 2007; Li et al., 1997) has exhumed several well-exposed sedimentary sections.

In this paper, we utilize extant Chinese nomenclature to subdivide the range previously referred to simply as the "Laji Shan" (Lease et al., 2007) into three segments. This subdivision reflects the different structural orientations, uplift/erosion histories, and geology of the constituent ranges—from northwest to southeast (Fig. 1B), the Riyue Shan, the Laji Shan, and the Jishi Shan. The Xunhua Basin, the focus of our study, is bordered on all sides by ranges bounded by thrust faults: the narrow ranges of the Laji Shan to the north, the Jishi Shan to the east, and the Zamazari Shan to the west, as well as the wider, more substantive West Qinling to the south (Fig. 1B). Key aspects of the growth of several of these ranges have been previously examined. The Eocene onset of reverse faulting in the West Qinling defined the contemporaneous plateau margin (Clark et al., 2010), whereas Miocene faulting northward of this margin initiated in the WNW-trending Laji Shan ca. 22 Ma and in the north-trending Jishi Shan ca. 13 Ma (Lease et al., 2011) (Fig. 1B). Erosion of the NW-trending Riyue Shan north of Guide Basin intensified after 10 Ma (Fang et al., 2005; Lease et al., 2007; note, in earlier publications, the Riyue Shan were referred to simply as the "Laji Shan"). The response of the Xunhua Basin to uplift of these ranges of various sizes and orientations, however, has been largely unconstrained. Thus, our study focuses on Xunhua Basin development in the northeastern corner of the basin adjacent to both the Laji Shan and Jishi Shan ranges.

The known Mesozoic–Cenozoic depositional record of northeastern Tibet in the Xining-Lanzhou region to the north, east, and west of Xunhua Basin is characterized by quite slow rates of accumulation (~40 m/m.y.) in a Lower Cretaceous (extensional?) basin (Horton et al., 2004), followed by slower, but relatively steady Eocene-to-early Miocene accumulation (~20 m/m.y.) in a foreland basin (Dai et al., 2006). Accelerated late Miocene–Pliocene accumulation (>100 m/m.y.) in the Guide Basin (Fang et al., 2005) has been interpreted to indicate accelerated local rock uplift (Lease et al., 2007).

Eocene–Oligocene deposition in the Xining Basin (Dai et al., 2006) occurred primarily within playa and marginal lacustrine environments (Abels et al., 2011; Dupont-Nivet et al., 2007) that were limited in spatial extent. Clastic input and inferred aridity generally increase

within the younger deposits. Lower Miocene deposits in the southern Xunhua Basin generally fine upward from sandy deltaic/floodplain facies to silt- and clay-rich lacustrine facies (Hough et al., 2011). Upper Miocene–Pliocene deposits in southern Xunhua, on the other hand, display a coarsening-upward trend from lacustrine facies to braided fluvial facies. Miocene–Pliocene stratigraphic records from the nearby Linxia and Guide Basins show similar depositional environments and coarsening-upward trends (Fang et al., 2003, 2005).

CENOZOIC STRATIGRAPHY

We measured and described ~2300 m of Tertiary sedimentary rocks (Fig. 2) in a continuous succession (the Hualong section) in the northeastern part of Xunhua Basin (Fig. 1B) near the town of Qiajia (section base: 35.981°N, 102.510°E; section top: 36.016°N, 102.505°E). The succession lies adjacent to the eastern Laji Shan–northern Jishi Shan and records the late Oligocene–Miocene growth of these ranges. Sedimentary rocks in the Hualong section are interpreted to have been deposited within five sedimentary environments (playa, marginal lacustrine/deltaic plain, alluvial fan, braided fluvial, floodplain) that exhibit a generally coarsening-upward trend. Next, we describe the lithologies found in the Hualong section in the context of five depositional facies that make up three overarching stratigraphic units.

At the base of the section (0–290 m; Fig. 2), facies A is composed of massive red-brown gypsiferous mudstone that is interbedded with gray-green laminated siltstone and green-white layered gypsum (up to 3 m thick). The gypsiferous mudstone is mildy calcareous to noncalcareous with abundant interstitial gypsum and gypsum veins (Fm, Table 1) and local gypsum flowers, blades, and gypsarenite layers. Mudstone beds are 0.1–30 m thick, tabular, and laterally continuous over tens to hundreds of meters. Most gypsum beds are 0.5 to 30 cm thick, tabular, and laterally continuous over meters to >100 m (E, Table 1). Clasts coarser than very fine sand are chiefly composed of gypsum crystals from either primary or secondary precipitation. The weathering of layers varies from blocky (0–50 m) to hackly (50–125 m) to cliff-forming (125–290 m), with a series of cliffs and ledges (125–290 m) defined by gypsum-rich layers. We interpret facies A (Table 2) to have been deposited in a shallow lacustrine environment with playa-like conditions (Schreiber and El Tabakh, 2000; Talbot and Allen, 1996) based on the presence of extensive primary gypsum beds in combination with both oxidized and reduced gypsiferous muds (Fig. 2).

Facies B deposits, located at 290–1070 m and 1160–1250 m height, consist of massive red-brown gypsiferous mudstone with interbedded tan sandstone and gray-green siltstone (Fig. 2). The mudstone has abundant gypsum veins and is otherwise similar in character to the mudstone (Fm, Table 1) described in the playa facies, with minor differences. Gypsum decreases in abundance up section, with layered gypsum becoming rare above 400 m and gypsum veins rare above 840 m. Mudstone found above 550 m, on the other hand, is characterized by gray-green to blue-green mottling, which increases in abundance up section. Finally, 0.3–1-m-thick interbeds of medium- to coarse-grained, tan sandstone that commonly exhibits trough cross-stratification (St, Table 1) occur throughout the entire interval (Fig. 2). Individual lenticular sandstone interbeds are stacked to form restricted lenticular bodies that are generally <5 m thick and extend laterally for <10 m. Horizontal laminations (Sh, Table 1) characterize the sandstone interlayers found between 450 and 650 m.

The lithologies we group together as facies B (Table 2) are interpreted to represent diverse depositional characteristics. Thick intervals of dominantly red-brown mudstone with abundant mottling extending for tens to hundred of meters of vertical section (Fig. 2) suggest prolonged floodplain, mud flat, or lacustrine deposition, though ubiquitous gypsum veins obfuscate a more detailed analysis of mudstone sedimentology. Intervals of alternating blue-green and red-brown siltstones (Fig. 2), on the other hand, suggest periodic subaerial conditions, and rare primary gypsum indicates occasional evaporative conditions. Additionally, distinctive fluvial channel sands commonly punctuate the fine-grained deposits (Fig. 2) and are restricted laterally to only a few meters, suggesting ribbon channel bodies incised into a muddy plain (Friend et al., 1979). Collectively, we interpret this diverse facies assemblage (facies B, Table 2) to be suggestive of intermittent floodplain, shallow lacustrine, and distributary channels as part of a deltaic plain/marginal lacustrine environment (Cabrera et al., 1985; Reading and Collinson, 1996).

Facies C contains brown and red-brown conglomerates and sandstones with interbedded mudstone arranged in several fining-upward successions (up to 10 m thick). These deposits are restricted to the middle of the section at 1070–1160 m height (Fig. 2). Conglomerate beds are typically massive, matrix supported, and have nonerosive bases (Cmm, Table 1). Commonly, subangular pebbles up to 40 cm diameter are enclosed in a medium- to coarse-grained sand matrix. Sandstone beds are 0.5–1.5 m thick, medium grained, and have
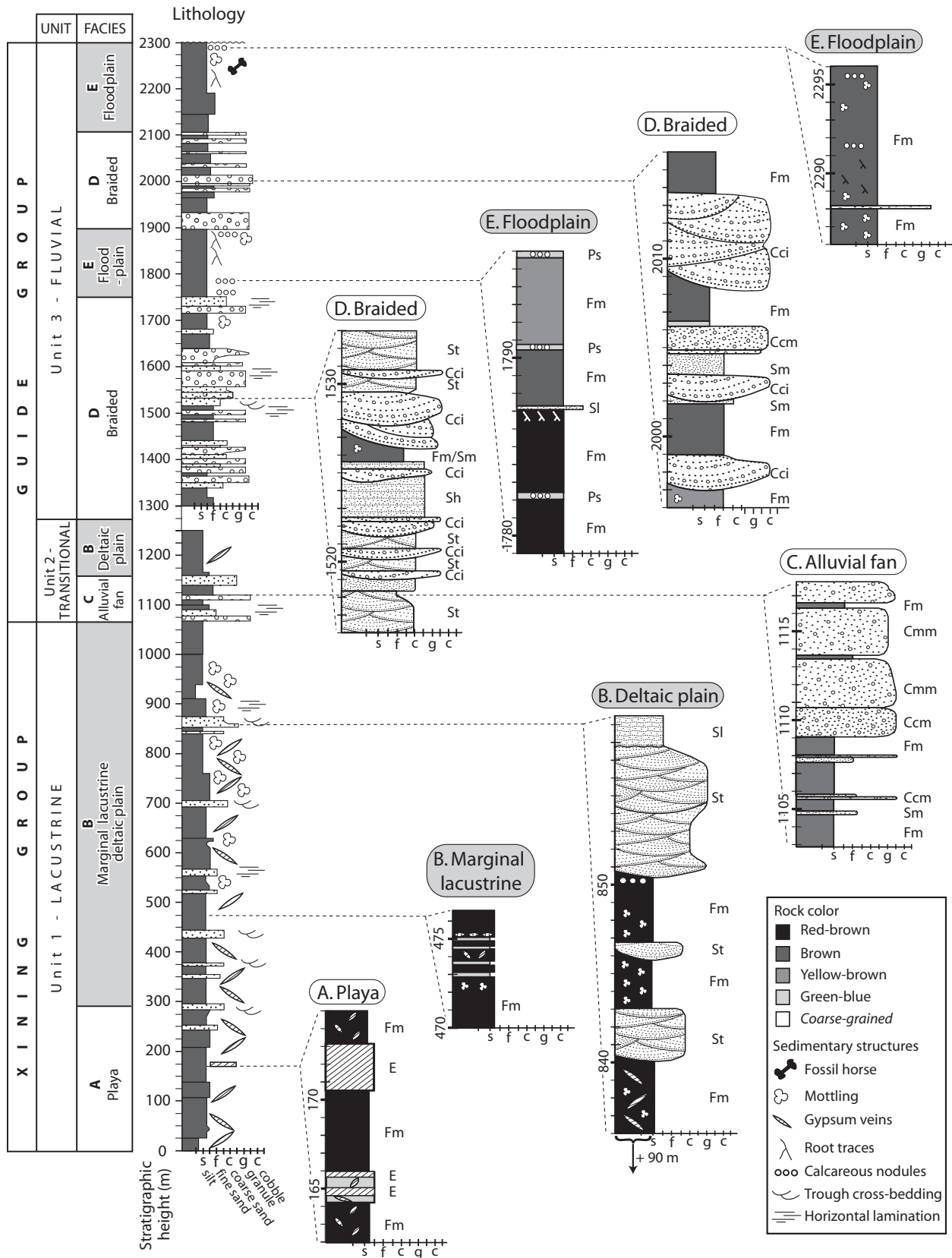
Figure 2. Lithologies and interpreted depositional facies and units within the measured Hualong magnetostratigraphic section from the northeastern margin of Xunhua Basin. Facies code abbreviations are described in Table 1. Expanded columns A to F illustrate typical facies assemblages for each depositional environment (see Table 2).

TABLE 1. LITHOFACIES AND INTERPRETATIONS USED IN THIS STUDY

Lithofacies code	Description	Interpretation
E	Layered gypsum beds	Chemical precipitation in an evaporative lake
Ps	Carbonate with pedogenic features including nodules and adjacent root traces	Soil formation on floodplain
Fm	Massive mudstone to fine-grained sandstone with common gray mottling and gypsum veins	Suspension settling in lake and overbank deposits
Sm	Massive medium- to fine-grained sandstone	Sandy mud flows and suspension settling in lake and overbank deposits
Sr	Fine- to medium-grained sandstone with small, asymmetric, 2D and 3D current ripples	Migration of small 2D and 3D ripples under weak (~20–40 cm/s), unidirectional flows in shallow channels
St	Medium- to very coarse-grained sandstone with trough cross-stratification	Migration of large 3D ripples (dunes) under moderately powerful (40–100 cm/s) unidirectional flows in large channels
Sp	Medium- to very coarse-grained sandstone with planar cross-stratification	Migration of large 2D ripples under moderately powerful (~40–60 cm/s), unidirectional channelized flows; migration of sandy transverse bars
Sh	Fine- to medium-grained sandstone with plane-parallel lamination	Upper plane bed conditions under unidirectional flows, either strong (>100 cm/s) or very shallow
Ccm	Pebble to cobble conglomerate, clast-supported, unstratified, disorganized to poorly sorted	Deposition from sheetfloods and clast-rich debris flows
Cci	Pebble to cobble conglomerate, clast-supported, horizontally stratified, imbricated, poorly sorted	Deposition from shallow traction currents in longitudinal bars and gravel sheets
Cmm	Massive, matrix-supported pebble to cobble conglomerate, poorly sorted, disorganized, unstratified	Deposition by cohesive mud-matrix debris flows

Note: Modified after Miall (1978) and DeCelles et al. (1991).

TABLE 2. DEPOSITIONAL FACIES AND ASSOCIATED FACIES CODES (FROM TABLE 1)

Depositional facies	Major facies codes	Minor facies codes
A. Playa	Fm	Sm, E, Sh, Fl
B. Marginal lacustrine/deltaic plain	Fm	Sm, St, Sh, Fl
C. Alluvial fan	Cmm, Fm, Ccm	Sh, Sm, St
D. Braided fluvial	Cci, Ccm, Sm, Fm	Cmm, Sh, St, Sr
E. Floodplain	Fm	Sm, Ccm, Sh, Cci, Ps, Sr

horizontal laminations (Sh, Table 1) and uncommon lenses (<0.2 m thick) of matrix-supported pebble conglomerate. Individual conglomerate and sandstone beds are laterally continuous over several to tens of meters, with stacked beds forming larger bodies that are laterally continuous over tens to hundreds of meters. We interpret facies C (Table 2) to have been deposited largely by mass flows (Nemec and Steel, 1984) in an alluvial-fan environment (Blair and McPherson, 1992) based on the general lack of stratification and channelization, nonerosive bases, matrix support, and textural immaturity of the deposits. Further investigation is needed to ascertain the types of mass flows (i.e., debris versus hyperconcentrated) that are dominant.

Fluvial deposits of facies D are found in the upper half of the section at 1300–1750 m and 1900–2110 m height (Fig. 2) and consist of conglomerates and sandstones with interbedded silty fine-grained sandstone. The conglomerates consist of subangular granules and pebbles that are typically clast-supported and imbricated (Cci, Table 1). Clasts are generally 0.5–2 cm in diameter within a poorly sorted matrix of sand, silt, and clay. Conglomerate channel scours are commonly 10–50 cm deep, and fining-upward successions (from cobble to pebble and pebble to medium sand) are up to 1–2 m thick. Conglomerate beds are 0.2–1 m thick, lenticular, and often pinch out over several meters. Individual beds stack to form lenticular bodies that are 1–5 m thick and laterally continuous over tens of meters. Clast roundness increases up section. Sandstones (Fig. 2) are typically medium grained and massive (Sm, Table 1), and they contain common horizontal laminations (Sh) and rare trough cross-stratification (St) and ripple marks (Sr).

Sandstone beds are laterally continuous over tens of meters, and bodies composed of several beds are continuous over hundreds of meters. Brown, silty, fine-sand interlayers are largely featureless, with mottling, rare floating granules and pebbles, and poorly developed pedogenic structures (Fm, Table 1). We interpret this facies association (facies D, Table 2) to represent a braided fluvial environment (Miall, 1996), based on the widespread channelization of conglomerates and sandstones together with evidence of interfluvial pedogenesis. The textural immaturity of the conglomerates may suggest deposition by ephemeral (flashy) flooding (Nemec and Steel, 1984). Additionally, some conglomerate beds may have been deposited by clast-rich or hyperconcentrated flows.

Facies E consists of red-brown, brown, and yellow-brown, fine- to very fine-grained sandstone that is prevalent between 1750 and 1900 m and 2110–2310 m in the section (Fig. 2). Minor conglomerate and medium- to coarse-grained sandstone interlayers also occur in this interval. The fine-grained sandstones are massive, 1–20-m-thick, tabular beds that extend laterally for tens to hundreds of meters and contain abundant root traces and gray mottling with rare burrows and floating granules (Fm, Table 1; Fig. 2). Uncommon calcrete and calcareous nodules define several prominent 30-cm-thick, white-green beds (Ps, Table 1) at heights of ~1780 m

and ~2310 m and are laterally continuous over tens of meters (Fig. 2). Interlayers of medium- to coarse-grained sandstone and clast-supported pebble conglomerate are 0.1–2 m thick, massive to horizontally laminated, and laterally continuous over meters to tens of meters. These coarse deposits exhibit poorly defined normal grading and define a series of minor channel fills. We interpret facies E (Table 2) to have been deposited in a fluvial floodplain environment (Collinson, 1996; Nanson and Croke, 1992) in which carbonate-rich paleosols developed on stable or slowly aggrading floodplains (Mack et al., 1993).

We divide the 2310 m Hualong stratigraphic section into three broad depositional categories based on the facies associations described here. From the bottom to the top of the section, the Hualong units are (1) lacustrine, (2) transitional, and (3) fluvial. Lacustrine unit 1 constitutes the bottom half of the section at 0–1070 m height and is composed of facies A playa deposits and facies B marginal lacustrine/deltaic plain deposits. We define a brief interval of facies C alluvial-fan and facies B deposits at 1070–1250 height as transitional unit 2. The upper half of the section (1300–2310 m) comprises fluvial unit 3 and contains alternating facies D braided stream and facies E floodplain deposits. Within a broad regional framework, lacustrine unit 1 likely correlates with the "Xining Group,"

whereas transitional unit 2 and fluvial unit 3 collectively correlate to the "Guide Group" (for descriptions, see Zhai and Cai, 1984; Fang et al., 2005; Dai et al., 2006; and references therein).

Paleocurrent and clast count measurements were obtained for conglomerates in units 2 and 3 (Fig. 3); no measurements were obtained from unit 1 and the lower half of the section. Each of the seven paleocurrent sites contains measurements from only ~10 imbricated pebble clasts. Measurements from four sites between 1360 and 1730 m show variable approximately southwestward paleoflow ranging from west-northwestward to southeastward. Three paleocurrent sites located between 1850 and 2050 m, on the other hand, show a more consistent westward paleoflow direction.

Observations of 100 clast lithologies from each of four sites between 1100 and 2050 m reveal no major changes in clast provenance. All sites are dominated by fine-grained shale and sandstone (79%–91%) with minor basement lithologies (Fig. 3). Granite and gneiss clasts together with potassium feldspar phenocrysts comprise 6%–15% of clasts, with 0%–6% vein quartz also present as angular to subangular clasts. None of these lithologies is

paleogeographically unique: Rocks of similar fine-grained and basement lithologies crop out on all sides of the basin (QBGMR, 1991). Despite their similar lithologic characteristics, however, rocks on various sides of the basin have different ages. Therefore, we use detrital zircon age distributions to precisely characterize different sediment sources and track their evolution within the entire stratigraphic succession (see Detrital Zircon Provenance section).

## MAGNETOSTRATIGRAPHY

Methods

We collected samples for magnetic polarity stratigraphy in mudstones, siltstones, and uncommonly sandstones from the Hualong stratigraphic section (Fig. 2). We drilled 1747 cores from 510 sites spanning ~1900 m for an average sampling site spacing of 3.7 m/site. All 2.5-cm-diameter core specimens were obtained in situ using a gas-powered drill. Remanent magnetizations were measured using a 2G Enterprises DC SQuID three-axis cryogenic magnetometer housed in a magnetically shielded room at the California Institute of Technology. The magne-

tometer has a background noise of <1 pAm^2 and is equipped with computer-controlled alternating field (AF) demagnetization coils and an automated vacuum pick-and-put sample changer (Kirschvink et al., 2008). Thermal demagnetization was performed in a magnetically shielded ASC™ oven in a nitrogen atmosphere.

One specimen from each site plus 77 duplicates from certain sites were analyzed using a combination of thermal and AF demagnetization techniques. All 587 specimens were initially measured for natural remanent magnetization (NRM) and then cooled in a LN$_2$ bath to remove potential multidomain viscous magnetizations. Specimens were subsequently subjected first to AF demagnetization in 2.5 mT steps up to 10 mT to remove low-coercivity magnetizations, and then to stepwise thermal demagnetization in 8–12 steps between a 150–250 °C starting temperature and a 600–680 °C ending temperature, typically in (1) 100–150 °C steps up to 450 °C, and (2) 15–50 °C steps up to 680 °C (Fig. 4). At least one specimen from every site was demagnetized, with second and third specimens also demagnetized if the initial specimen yielded unstable directions or was bracketed by samples from adjacent sites with opposite polarity.

Our 2310-m-thick Hualong magnetostratigraphic section is a composite of several shorter subsections, as is typical of many stratigraphic studies (see GSA Data Repository Fig. DR1 for sampling map[1]). We utilized prominent marker beds to translate over short distances of a few hundred meters or less. Remeasurement of the section during detailed stratigraphic analysis and comparison of magnetostratigraphies on either side of the subsections, however, revealed three errors in our initial subsection correlations. Each of these errors was made in a place where correlations over large distances (~1 km) were necessary, and the errors are due to the difficulty of correlating over rugged terrain. We discuss these stratigraphic corrections both for transparency and so that subsequent studies can reassess these correlations. We discovered an ~150-m-wide gap in the magnetostratigraphy centered near 450 m height, an ~45-m-wide gap centered at 1275 m height, and an additional ~68 m of overlap at a portion of the section centered at ~2000 m. The stratigraphic section that we present (Fig. 2) reflects these corrections. The basal 200 m interval of our measured section was too friable and dissected by gypsum veins to permit reliable magnetostratigraphic sampling.

Figure 3. Clast counts and paleocurrent (imbrication) measurements from the Hualong magnetostratigraphic section. Paleocurrent measurements are corrected for fold plunge followed by bedding dip; *n* = number of clasts measured.
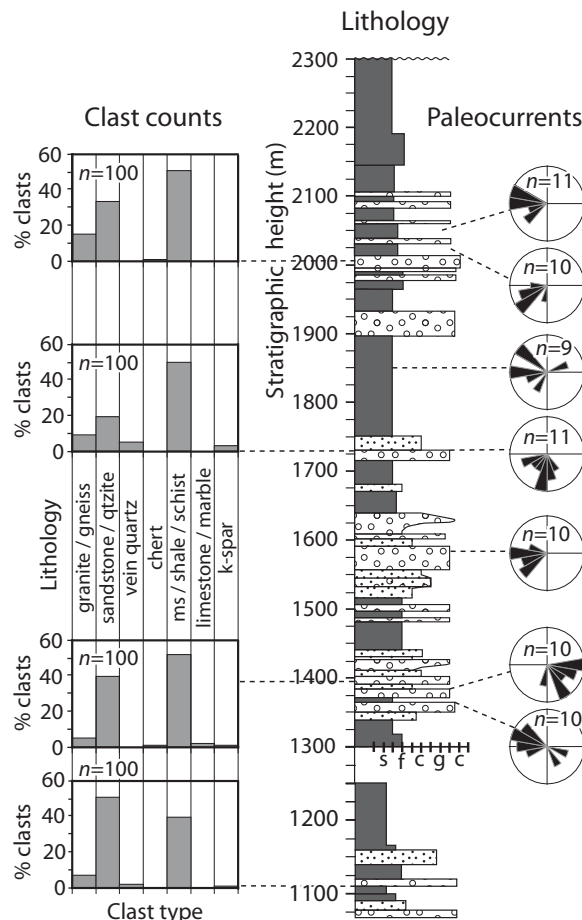
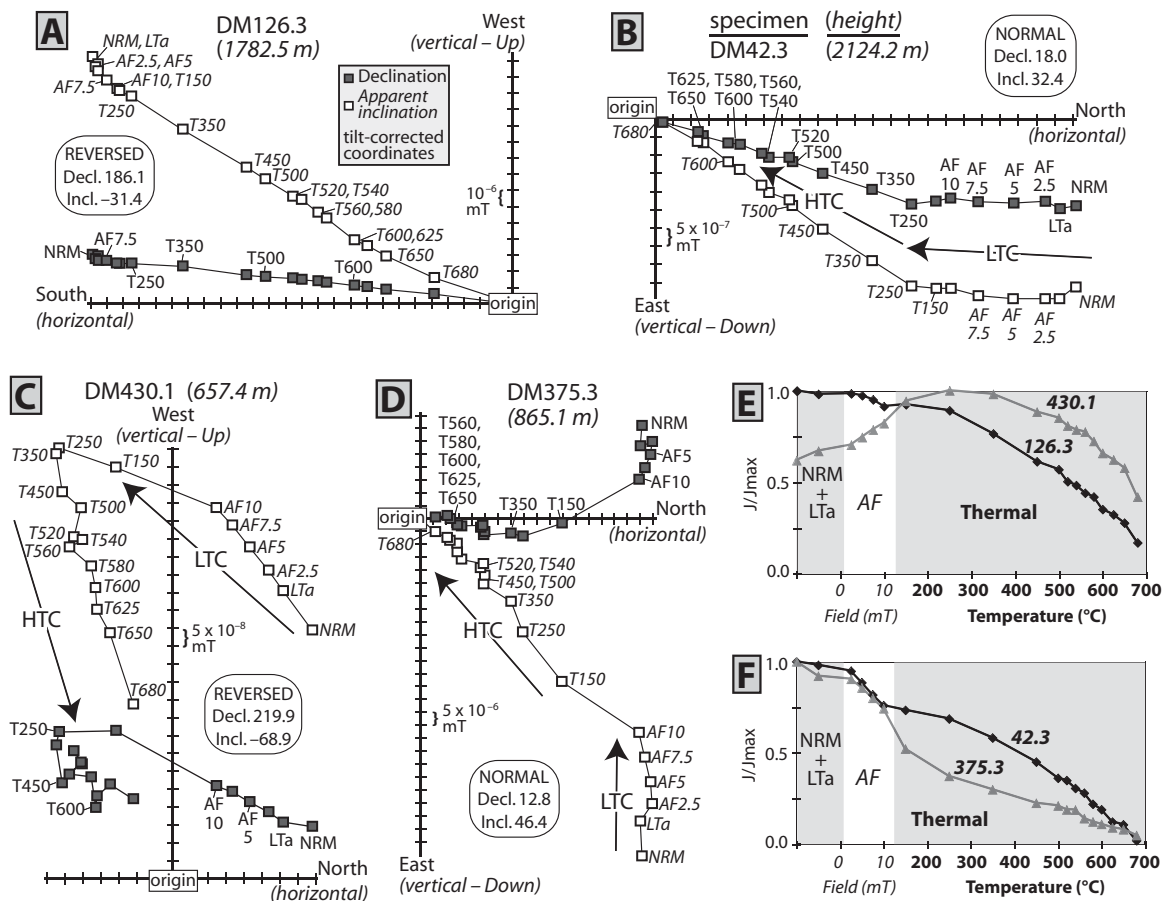*Oligocene–Miocene basin evolution on the northeastern Tibetan Plateau*

Figure 4. (A–D) Representative orthogonal demagnetization plots for specimens from the Hualong magnetostratigraphic section. Results are from stepwise alternating-field and thermal demagnetization steps. Plots show a low-temperature component (LTC) that is typically removed by 250 °C and interpreted to be a viscous overprint, as well as a high-temperature component (HTC) that is interpreted to be the characteristic remanent magnetization. Note that the intensity scale varies ~100-fold. (E–F) Decay of magnetic moment for the same specimens during demagnetization. NRM—natural remanent magnetization, LTa—"low-temperature" step (samples cooled in liquid nitrogen), AF—alternating field (in mT), T—temperature (in °C).

Results

The intensity of the NRM for Hualong specimens is typically 10^{-2} A/m, with a range of 10^{-1}–10^{-3} A/m. After LN_2 treatment, specimens typically displayed a drop in magnetic intensity of <15%, indicating that no appreciable remanence was carried by multidomain magnetite or hematite (Figs. 4E and 4F). Our stepwise demagnetization procedure clearly resolves a low-coercivity, low-temperature component and a high-temperature component (Fig. 4). The low-temperature component is typically removed by 250 °C (Figs. 4B, 4C, and 4D), but sometimes not until 450 °C. The low-temperature component does not typically decay toward the origin and is interpreted to be a viscous overprint.

The high-temperature component decays toward the origin, typically exhibits stable behavior until 650–680 °C, and is interpreted to

reflect the characteristic remanent magnetization (ChRM). Progressive unblocking of the high-temperature component between 250 °C and 580 °C suggests a magnetite carrier. Complete unblocking of the high-temperature component by 680 °C, however, indicates that a hematite carrier is also present (Fig. 4). Furthermore, coercivity spectrum analyses of isothermal remanent magnetism (IRM; Fig. DR2 [see footnote 1]) for selected Hualong specimens generally show gradual, continual acquisition of IRM with increasing field strength—a behavior consistent with a hematite carrier. A small drop in remanence at ~580 °C in many specimens (Fig. 4E) and a protracted interval of relatively rapid IRM acquisition before ~70 mT for some IRM samples (Fig. DR2 [see footnote 1]), however, suggest a magnetite carrier as well. When both magnetite and hematite are present in the same specimen, no significant

difference in remanent direction is observed when comparing the 250–580 °C portion of the unblocking spectrum with the 600–680 °C portion (Fig. 4). This behavior suggests that both magnetite and hematite recorded the same paleomagnetic field when their remanent directions became fixed in the rock.

ChRM directions were determined for each specimen using principal component analysis (Kirschvink, 1980) as implemented in Paleo-Mag 3.1.0 b1 (Jones, 2002), typically from nine points (minimum 3 points, maximum 20) from the stable high-temperature component. The origin is only included if the demagnetization path decays toward it. We report ChRM directions in stratigraphic coordinates that are corrected for fold plunge followed by bedding tilt (Fig. 5) because we mapped a series of folds within the Hualong sections with axes that plunge ~25° in the direction of N17°E. Paleocurrent imbrication
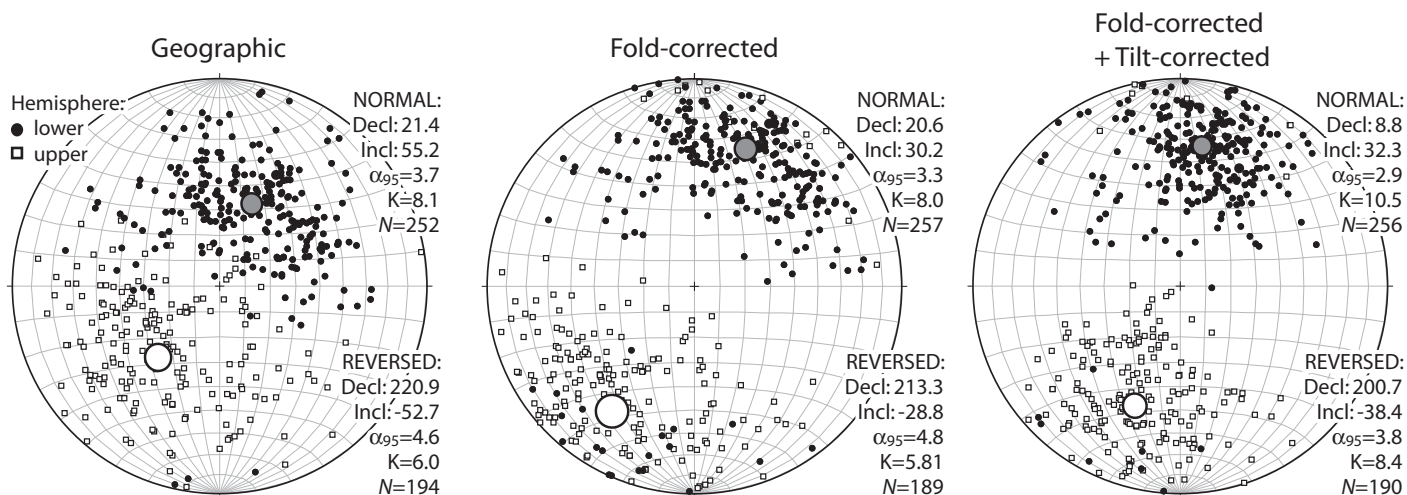
Figure 5. Stereographic equal-area plots of characteristic remanent magnetization directions from the Hualong section in geographic, fold-corrected, and fold- and tilt-corrected coordinates. Black circles are plotted in the lower hemisphere, and white squares are plotted in the upper hemisphere. Larger circles indicate α_{95} error around the Fisher mean with mean data listed adjacent to each plot. Different N values reflect a few low-latitude specimens that change polarity when fold and tilt corrections are applied. The Hualong data fail the reversal test (McFadden and McElhinny, 1990), likely due to an unremoved partial normal overprint that biases reversed directions to more westerly orientations.

measurements are also subject to this two-stage untilting procedure.

Virtual geomagnetic poles (VGP) were then calculated and their latitude used to denote either a normal polarity or reversed polarity specimen. Specimens with a noisy or ambiguous orthogonal demagnetization diagram or a maximum angular deviation (MAD) >15% are excluded from further analysis, thus removing 23% of the measured specimens. The average MAD for resulting specimens is 6°. A positive fold test (Tauxe and Watson, 1994, as implemented in Tauxe et al., 2009) attests to the reliability of our demagnetization data in defining the depositional remanence (Fig. 6). Progressive untilting of the individual fold-corrected ChRM directions about the local bedding orientation shows the maximum clustering of directions oc-

curring at 108% untilting, with 95% confidence limits of 97%–122% untilting (Fig. 6). It is worth noting that without the additional correction for the fold plunge, the data set fails the fold test. Clearly, for folds with plunges >5°–10°, a two-step unfolding procedure is warranted.

The Hualong paleomagnetic data set, however, has a negative reversal test (McFadden and McElhinny, 1990), with the paleomagnetic data set (Fig. 5) failing both as a whole and when divided into 10 regularly spaced sub–data sets (7 of 10 sub–data sets fail). The negative reversal test suggests an unremoved overprint. Reversed directions are biased toward more westerly directions, and normal directions are biased toward more northerly directions, as expected from the effect of an unresolved partial normal overprint, e.g., figure 7 of Dupont-Nivet

et al. (2008). Given the significant remanence retained by some samples even at 680 °C, e.g., sample DM430.1 (Fig. 4C), a residual overprint is not unexpected. In addition, inclination shallowing, common in central Asia sedimentary strata, e.g., Gilder et al. (2003), is suggested for the Hualong paleomagnetic data set by mean corrected inclinations (32°–38°; Fig. 5) that are much lower than expected: 56°–59°, calculated from late Oligocene–late Miocene Eurasian reference poles in Besse and Courtillot (2002). Given that inclination shallowing occurs early during sedimentation, its presence in the Hualong data set suggests a primary origin for the measured magnetic remanence.

Given the success of the fold test, the presence of inclination shallowing, and the fact that normal and reversed directions all plot within their respective hemispheres (indicating that the sample populations are qualitatively antipodal), we accept our polarity determinations despite the failure of the reversal test. We acknowledge that a partial overprint remains unremoved, however, and suggest that it would be unwise to utilize the Hualong paleomagnetic data set to study rotations within the basin. The success of the fold test and the failure of the reversal test, when considered together, suggest that the partial normal overprint affected many Hualong sites and likely occurred after deposition of the youngest unit within the section.

We constructed a detailed magnetic polarity stratigraphy based on the VGP latitudes from the Hualong paleomagnetic data set (Fig. 7).

Figure 6. Positive fold test for Hualong characteristic remanent magnetization (ChRM) directions shown by the 95% confidence interval for τ_1 overlapping with 100% untilting of ChRM vectors corrected for strata orientation (Tauxe et al., 2009; Tauxe and Watson, 1994). The τ_1 maximum reflects the tightest grouping of the ChRM directions during progressive untilting of the strata and is defined by the eigenvalues of the orientation matrix.

Oligocene–Miocene basin evolution on the northeastern Tibetan Plateau
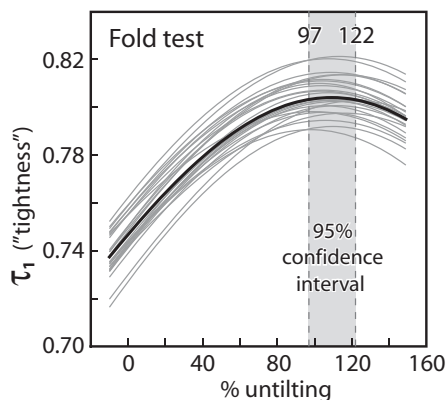
We identified 33 normal magnetozones and 31 reversed magnetozones in the Hualong section, with each magnetozone defined by two or more specimens that display the same polarity and have VGP latitudes >30°. A jackknife re-sampling of our magnetostratigraphy affirms the robustness of our data set, returning a J value of −0.40, which lies within the recommended range of 0 to −0.5 (Tauxe and Gallet, 1991; Fig. DR3 [see footnote 1]). This result suggests that we have recovered more than 95% of the true number of magnetochrons. Additionally, a statistical assessment (Johnson and Mcgee, 1983) of the number of reversals expected with our site density (63) is commensurate with the number of reversals we detected (65). Questionable reversals defined by only a single specimen are shown with a half-bar (Fig. 7).

The correlation of the Hualong magnetic polarity stratigraphy to the geomagnetic polarity time scale (GPTS: Ogg and Smith, 2004) is facilitated by our discovery of an in situ fossil jawbone complete with teeth from a Miocene horse. We recovered the fossil within our measured stratigraphic section during the course of sample collection. The teeth (Fig. 8) are identified as belonging to the *Hipparion weihoense* taxon with an age of 9.7–8.7 Ma (early part of the late Miocene, NMU 9 of Bahean or MN 10 of Vallesian; Deng, 2008, personal commun.). The presence of the fossil specimen *within* our magnetostratigraphic section is fortuitous, because it eliminates potential error that arises when correlating fossil-bearing strata across several to tens of kilometers, which is a particularly valid concern in the Xunhua region due to the presence of rapid lateral variations in both facies and thicknesses, e.g., Fang et al. (2003).

The *Hipparion weihoense* specimen serves as an independent chronostratigraphic tie point that anchors the top of the Hualong magnetostratigraphy to the GPTS (Fig. 7). For our preferred correlation of the Hualong magnetic polarity
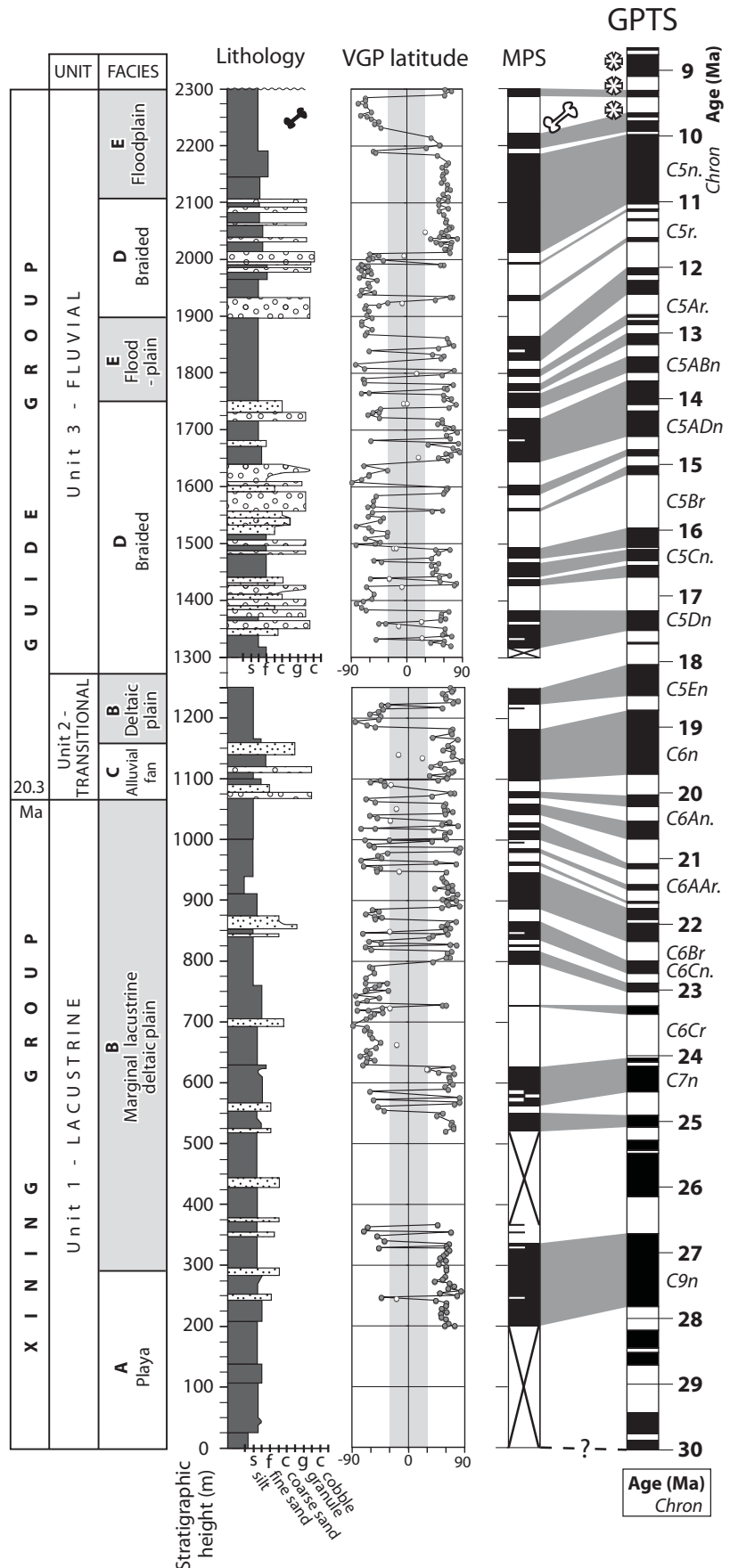
Figure 7. Hualong section magnetic polarity stratigraphy (MPS) and its correlation to the geomagnetic polarity time scale (GPTS; Ogg and Smith, 2004). Stratigraphic logs of virtual geomagnetic pole (VGP) latitudes, lithologies, and depositional units are shown on left. Each magnetozone in the magnetic polarity stratigraphy is defined by two or more specimens (typically from multiple sites, but sometimes from one site) of the same polarity that have VGP latitudes >30°. Questionable reversals defined only by a single specimen measured from one site are labeled with half-bars.

Figure 8. *Hipparion weihoense* **teeth discovered from the top of the upper Hualong section at ~2250 m. The five cheek teeth belong to the same individual: right upper second, third, and fourth premolars and first molar (P2, P3, P4, M1); and the right lower fourth premolar (p4). The teeth are charac-**

Hipparion weihoense NMU 9 of Bahean or MN 10 of Vallesian

M1 P4 P3 P2

2 cm p4 early Late Miocene 9.7–8.7 Ma

terized by strongly convex labial walls, rounded and long double-knots (metaconid and metastylid), more lingually shifted than entoconid, and simple hypoconulid, without clear subdivision into two lobes. *Hipparion weihoense* **is a taxon from the early part of the late Miocene (NMU 9 of Bahean or MN 10 of Vallesian) with an age of 9.7–8.7 Ma (Deng, 2008, personal commun.).**
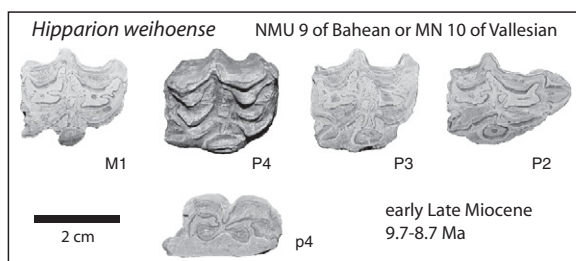
stratigraphy to the GPTS, the magnetostratigraphy spans 27.8–9.3 Ma. Depositional ages are assigned to the described lithologic units as follows: lacustrine unit 1 spans 30–20.3 Ma, transitional unit 2 spans 20.3–18 Ma, and fluvial unit 3 spans 18–9.3 Ma. Our correlation places the boundary between the Xining Group and Guide Group at 20.3 Ma.

The correlation of the Hualong magnetic polarity stratigraphy to the GPTS between 27.8 and 25 Ma contains some uncertainty because of the presence of a gap in our magnetostratigraphic sampling (between 370 and 520 m height in the section), plus several questionable single-site polarity reversals (Fig. 7). Some of the single-site reversals, however, might correlate with short-duration "cryptochrons" recognized within C7n and C9n (Cande and Kent, 1995; Tauxe and Hartl, 1997). Our proposed correlation for the 27.8–25 Ma portion of the section assumes no major accumulation rate changes and no major depositional hiatus: These assumptions are supported by the continuity of the overlying 25–9.3 Ma magnetostratigraphic record, as well as the absence of field evidence for an unconformity.

Finally, we acknowledge several, short-lived (i.e., <100 k.y.) polarity reversals that do not correlate between the GPTS time scale and the Hualong magnetic polarity stratigraphy record. We discuss these reversals later herein; however, their presence does not change the magnetostratigraphic correlation. First, there are five, short GPTS chrons that have no correlative magnetozone in the Hualong magnetic polarity stratigraphy: reversed chrons C4Ar.3r, C5Ar.2r, C6Bn.1r, and C7n.1r, plus normal chron C5r.2r-1. These uncorrelated GPTS chrons, which have durations of 30–60 k.y., could be due to the following: (1) Our sampling missed these chrons because the spacing between superposed samples represents a longer period of time than the short duration of each

chron, (2) the Hualong succession had depositional hiatuses during these short chrons, or (3) samples from these short, reversed polarity intervals were later overprinted with normal polarity. Second, we observe three magnetozones within the Hualong magnetic polarity stratigraphy that have no correlative chron on the GPTS: reversed magnetozones within C6AAn and C5Dn, plus a normal zone within C6Cn.1r. Assuming steady deposition on 1.5 m.y. time scales, the uncorrelated magnetozones have estimated durations of 20–100 k.y. These unexpected magnetic polarity stratigraphy magnetozones may be invalid and due to errors during sampling or laboratory analysis, or, alternatively, they might reflect unrecognized cryptochrons within the GPTS.

SUBSIDENCE

Both the detail and duration of the Hualong magnetostratigraphy make it ideal for determining variations in sediment accumulation rates for the northern Xunhua Basin from 27 to 9 Ma. We decompacted sediment thicknesses according to their observed lithologies following the methods and porosity values of Sclater and Christie (1980). We performed two separate decompaction routines—one with deposition ending at ca. 9 Ma (the top of our measured Hualong section) and a second with an additional 1000 m of deposition ending at ca. 2 Ma. Though the youngest strata in the Hualong section are 9 Ma, deposition in southern Xunhua and adjacent basins continued until ca. 3–1.8 Ma (Fang et al., 2003, 2005; Hough et al., 2011), when the Yellow River began incising headward through the region (Craddock et al., 2010; Harkins et al., 2007) and evacuating basins. The separate 9 Ma versus 2 Ma decompaction routines illuminate the range of possible late Miocene–Pliocene depositional histories for Hualong; it is likely that Hualong deposition continued uninter-

rupted until ca. 2 Ma, although the possibility that Hualong was abandoned as a depocenter ca. 9 Ma as local deformation propagated into the basin cannot be eliminated. If deposition did continue in Hualong from 9 until 2 Ma, extrapolation of accumulation rates and facies from our upper Hualong section and the upper Xunhua section (Hough et al., 2011) suggests an additional ~1000 m of fluviolacustrine deposition during this time.

Accumulation rates derived from the two different decompaction routines (9 Ma versus 2 Ma) display similar relative values and trends, differing only in absolute values by 11%–29%. Relatively steady accumulation at a rate of ~170 m/m.y. in Hualong between 27 and 24 Ma was followed by a distinct period of accelerated accumulation between 24 and 21 Ma with rates of ~200–310 m/m.y. (Figs. 9A and 9B). By 21 Ma, rates dropped to ~120 m/m.y. and remained steady until 12 Ma, when a distinct acceleration raised rates to ~200 m/m.y. until the top of the section at 9 Ma. The average decompacted accumulation rate for the entire section is 150 m/m.y. (9 Ma routine) to 180 m/m.y. (2 Ma routine). Sediment accumulation curves that have not been corrected for compaction also show distinct accelerations in rate at 24 and 12 Ma, with an average rate for the entire section of ~110 m/m.y. (Figs. 9A and 9B). We used compacted accumulation rates when comparing the Hualong section with sections from adjacent basins to maintain consistency with them (see Discussion).

To discriminate between the effects of tectonic versus sediment loading, we performed a one-dimensional Airy backstripping routine with exponential reduction of porosity using the method of Allen and Allen (2005) and sediment porosity values of Sclater and Christie (1980) as implemented in the OSXBackstrip program version 2.6 (Cardozo, 2009). We recognize that basin flexure was not the only control on Xunhua sediment accumulation rates; tectonic damming behind growing structures may also have been significant, particularly for the 12–9 Ma portion of the section. Thus, our backstripping results provide estimates of maximum sediment and tectonic loading rates; damming would diminish loading rates. We assumed sediment loading only (e.g., no water loading) because of the terrestrial, arid setting of Xunhua Basin. We also made the simplifying assumption that the elevation of the basin has remained constant for the duration of accumulation, given a lack of independent paleoelevation information.

Our backstripping results show accelerated subsidence until 21 Ma, when peak rates dropped three- to fourfold compared to the maximum rates at ca. 23 Ma (Fig. 9C). A protracted

Figure 9. (A) Age versus thickness for the Hualong magnetostratigraphic section. Curves depict both compacted and decompacted lithologies, plus separate decompaction routines run for deposition ending at 9 Ma and at 2 Ma. The latter assumes an extra 1 km of deposition prior to 2 Ma. Accumulation rates are slopes of linear regressions with % error indicating the α_{95} limits of regression. Vertical dashed lines are dividing lines between regressions. Note the accelerated accumulation rates at 24–21 Ma and at 12–9 Ma. (B) Age versus accumulation rate for the Hualong section. Blocky data reflect rates for each correlated magnetozone, and smoother data reflect a 2 m.y. moving average. (C) Age versus subsidence for the Hualong section from backstripping analysis. Subsidence rates are slopes of linear regressions with % error indicating α_{95} limits of regression. Range of rates for each age section reflects the separate "9 Ma" and "2 Ma" decompaction routines described in A. (D) Hualong section lithologies and depositional units versus age for reference with accumulation and subsidence plots above: A, B, and C. Note that (1) rapid accumulation rates at 24–21 Ma are coincident with deposition of fine-grained lacustrine unit 1; (2) progradation of coarse-grained units 2 and 3 is coincident with slow rates, suggesting that underfilled foreland deposition was controlled by subsidence and not supply; and (3) thickness scale is nonlinear.

period of rapid subsidence starting at 27 Ma intensified from 24 to 22.5 Ma and remained accelerated, though slower, until 21 Ma. Subsidence rates then decreased and remained stable from 21 to 12 Ma before accelerating 50%–75% from 12 to 9 Ma.

Our interpretations of first-order changes in subsidence rates at ca. 24, 21, and 12 Ma are insensitive to modifications of the backstripping routine such as the addition of a water load or an overlying Miocene–Pliocene sedimentary load. Inclusion of a large, 100-m-deep water load creates only a 1% increase in the magnitude of the relative changes in subsidence rate, although this water load increases the absolute subsidence rates by 43%–45% uniformly throughout the section. Adding an overlying 1000-m-thick, 9–2 Ma sedimentary load, as explored with our 2 Ma decompaction routine, gives relative subsidence values and trends that are similar to our 9 Ma routine (without the additional load), although the results differ absolutely by 10%–30% (Fig. 9C).
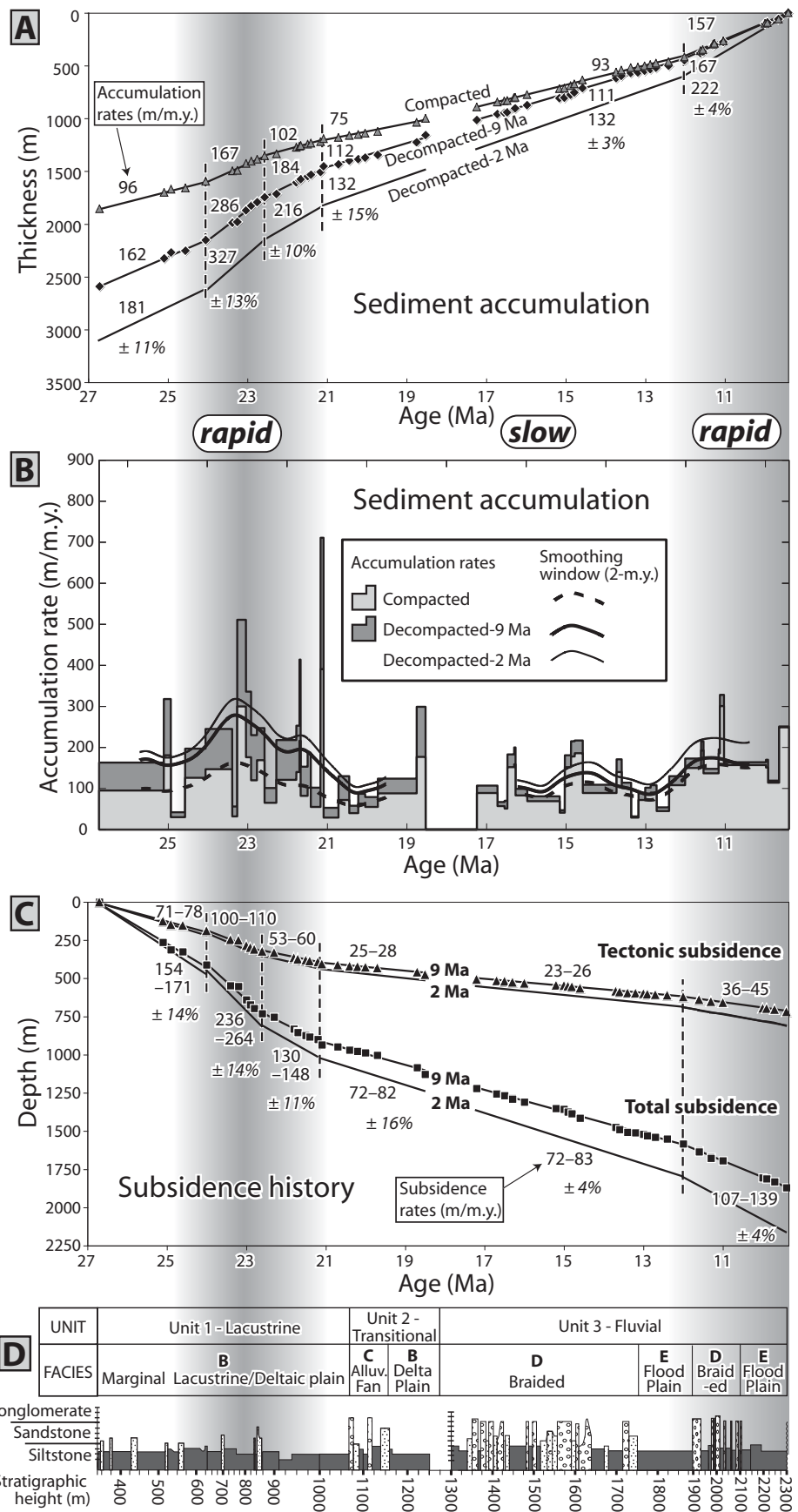
DETRITAL ZIRCON PROVENANCE

Methods

Provenance analyses using single-grain detrital zircon U-Pb age determinations have proven particularly useful in areas where two or more geographically distinct source areas have similar lithologies but have distinguishable U-Pb age signatures (DeCelles et al., 2004). The uplift and erosion of one range relative to other ranges can be assessed by examining detrital zircon age spectra from sediments deposited in basins adjacent to these ranges. Age spectra from several levels within a stratigraphic succession that spans several million years can track the evolution of source terranes and detect the emergence of newly uplifted ranges (Lease et al., 2007).

We collected ~5 kg sandstone samples from each of six stratigraphic horizons within our measured section from Hualong (Fig. 2). The age of each horizon is well constrained based on our detailed magnetostratigraphy, and overall these ages range from 28 to 10 Ma (Fig. 7). We also collected samples from five horizons within the Wangjiashan section in Linxia Basin, which has ages ranging from ca. 25 to 7.5 Ma based on magnetostratigraphic correlation (2–11 Ma; Fang et al., 2003) and lithostratigraphic correlation to the Maogou section (11–25 Ma; Li et al., 1997); samples from two of these horizons were analyzed previously (Lease et al., 2007). To preclude potential biasing of the zircon distribution by a poorly mixed depositional environment (DeGraaff-Surpless et al., 2003), each sample consists of several subsamples collected a few meters apart within the same stratum. We report detrital zircon age spectra from typically >95 single grains per sample. The Hualong stratigraphic succession is well suited for an analysis of local tectonism because it lies along the Laji-Jishi Shan range front and, therefore, is more likely to contain locally derived sediment and record the growth of nearby ranges.

To better characterize detrital zircon age signatures currently being supplied by various local rock units (source terranes) in the Laji-Jishi-Riyue Shan, we supplemented published work (Lease et al., 2007) with 294 additional single-grain analyses from four new samples (Fig. 1B). Each sample is composed of ~5 kg of sand from a modern catchment that drains one or more lithologic units. Our four new samples are from small catchments (<4 km^2) that are dominated by Proterozoic or Cretaceous units, neither of which has been documented to have a distinctive age signature. We sampled along the range front to avoid contamination by recycled zircon population from recently eroded Neogene strata.

U-Pb geochronology of detrital zircons was conducted by laser ablation–multicollector–inductively coupled plasma–mass spectrometry (LA-MC-ICP-MS) at the University of Arizona LaserChron Center (Gehrels et al., 2006). Measured ages and isotopic ratios are reported in the GSA Data Repository (see footnote 1).

Results I—Modern Source Terranes

Detrital zircon age populations from modern catchments can be tied to discrete source terranes within adjacent ranges. Modern catchments draining the Laji-Jishi-Riyue Shan are dominated by a 450 Ma zircon population derived from early Paleozoic plutonic and Cambrian volcanic units (labeled Pp and Cv), with a subsidiary ca. 850 Ma (or 500 to 1000 Ma) zircon population derived from a Silurian sedimentary unit (S) that is exposed locally (Fig. 10A; Lease et al., 2007). Our new analyses from catchments draining Proterozoic units (samples Pr2 and Pr3, Fig. 10A) show that they lack a dis-

tinctive age signature but instead are dominated by ca. 450 Ma zircons, likely from abundant granitic dikes within the unit.

Modern catchments draining the West Qinling are characterized by a discrete ca. 250 Ma zircon population derived from Triassic plutons (Tp) and a broader >1500 Ma population of recycled zircons derived from Triassic Songpan-Garze flysch (Tr; Fig. 10B; Lease et al., 2007). The Triassic Songpan-Garze unit (with its >1500 Ma Tr zircons) constitutes the majority of exposed rock in the West Qinling (Fig. 1B); however, Triassic flysch is not found immediately north, across the south Qilian suture (Yin and Harrison, 2000). North of the West Qinling, Triassic flysch is only present in a restricted area of the Riyue Shan (Fig. 1B), a distal area that is not a likely source area for the Xunhua or Linxia Basins, which are our focus. Thus, we interpret >1500 Ma Triassic flysch zircons found within the late Oligocene–Miocene Xunhua and Linxia Basin fills to be derived primarily from a proximal, West Qinling source.

Figure 10. Detrital zircon U/Pb age distributions from samples within modern catchments (locations in Fig. 1B) in the (A) Laji-Jishi-Riyue Shan and (B) West Qinling. Modern Laji-Jishi Shan samples are dominated by ca. 450 Ma and 500–1000 Ma zircon populations, which can be used to distinguish detritus eroding from the range. Modern West Qinling samples, in contrast, are characterized by ca. 250 Ma and >1500 Ma populations. Distributions are shown as probability density functions.
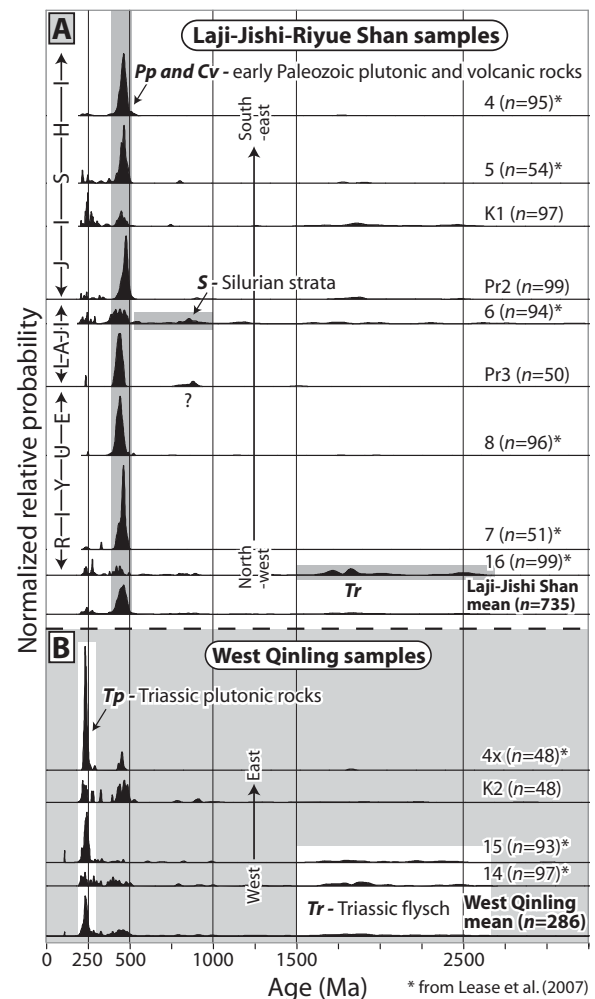
Our new analyses from catchments draining the Cretaceous unit in both the West Qinling (sample K2; Fig. 10B) and Laji-Jishi-Riyue Shan (sample K1; Fig. 10A) show that this unit exhibits a composite age spectra including all four documented local source terranes, and thus the Cretaceous unit cannot be distinguished as a unique source terrane. In addition, during mineral separation of modern detrital zircon samples, we observed that samples draining only Cretaceous bedrock (samples K1 and K2) had grain yields that were orders of magnitude lower than yields from samples draining plutonic and other lithologies. The much lower abundance of zircon grains from Cretaceous sources relative to other potential sources suggests that recycled zircons from Cretaceous sources are volumetrically insignificant and that late Oligocene–Miocene basin strata are dominated by other basement sources with a greater abundance of zircon grains.

Altogether, detritus derived from the Laji-Jishi-Riyue Shan, which lie to the north and east of Xunhua Basin, is best characterized by a 450 Ma early Paleozoic population that constitutes 62% of all modern detrital zircons dated from the range (Fig. 10A). This 450 Ma population constitutes 78% of Laji-Jishi-Riyue zircons when 2 of 9 modern samples are excluded from the range average: (1) sample 16 from the Riyue Shan, which contains Triassic flysch zircons that do not represent a viable northern source for the Xunhua and Linxia Basins, and (2) sample K1, which contains indistinguishable, volumetrically insignificant zircons from Cretaceous strata. In comparison, detritus derived from the West Qinling and Zamazari Shan, which lie to the south and west of Xunhua Basin, is best characterized by a 250 Ma Triassic plutonic population (43% of all modern detrital zircons) and >1500 Ma population (29%) from Triassic flysch (Fig. 10B).

Results II—Late Oligocene–Miocene Provenance

In the context of these contrasting source areas, the emergence of the eastern Laji Shan and Jishi Shan as important source areas can be discerned by comparing the U/Pb age distributions in strata from the northern edge of the Xunhua Basin contained within our Hualong magnetostratigraphic section (Fig. 11B). The age spectra for each stratigraphic horizon can be examined against a background of ca. 250 and >1500 Ma zircon age populations from the West Qinling, a range which has been eroding at a relatively steady rate of 0.1 mm/yr since ca. 45–50 Ma (Clark et al., 2010). The Hualong zircon spectra reveal a major transition in the northern Xunhua Basin between 22.5 and 19 Ma as dominant

Figure 11. (A) Age distributions from source terranes in the Laji-Jishi Shan and West Qinling shown for reference. (B–C) Detrital zircon U/Pb age distributions from magnetostratigraphic horizons within the (B) northern Xunhua (Hualong) Basin and (C) western Linxia Basin. Note enhanced abundance of Laji-Jishi Shan zircons in Xunhua Basin by 19 Ma and in Linxia Basin by 11.5 Ma, indicating intensified erosion of the Laji Shan and Jishi Shan, respectively. Wide, light-gray line in background portrays evolution of dominant zircon populations and highlights the doubling of the ca. 450 Ma Laji-Jishi Shan population by the middle of each section. Linxia Basin samples were collected from the Wangjiashan section with age assignments based on magnetostratigraphy (2–11 Ma; Fang et al., 2003) and lithostratigraphic correlation to the Maogou section (11–25 Ma; Li et al., 1997). Distributions are shown as probability density functions.
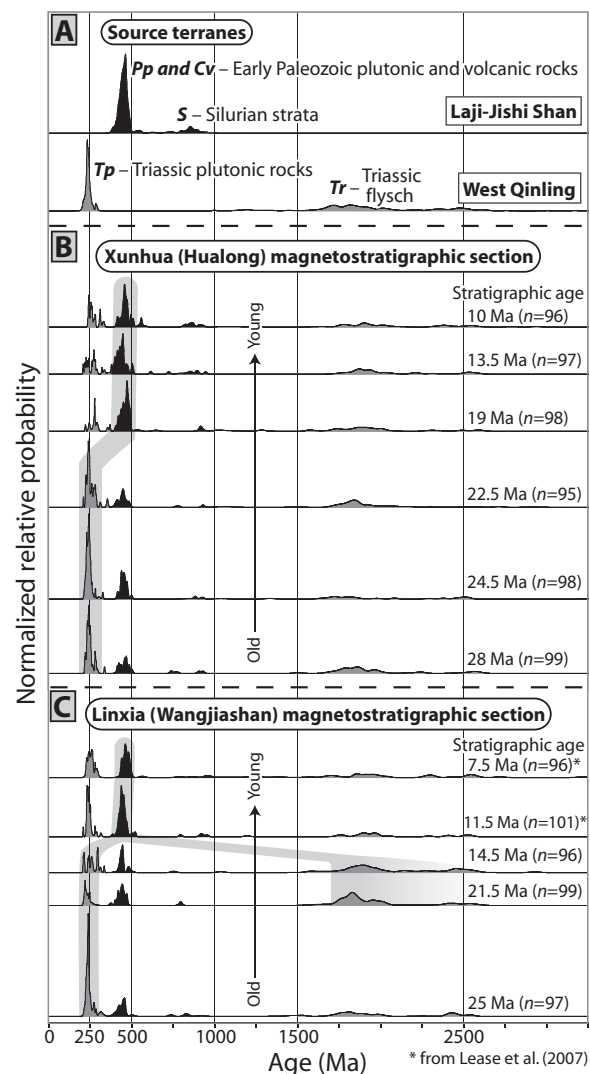
sources in the West Qinling were supplanted by sources in the Laji Shan–Jishi Shan (Fig. 11B).

To determine the combination of source terranes that best defines the age distribution of each stratum (Fig. 11B), we used a sediment-mixing model (Amidon et al., 2005; Lease et al., 2007) that includes our four primary source terranes (Fig. 11A): Triassic plutonic (Tp; ca. 250 Ma), Triassic flysch (Tr; >1500 Ma), early Paleozoic plutonic and volcanic (Pp and Cv; ca. 450 Ma), and Silurian sedimentary (S; 500–1000 Ma) units. For the range of possible source combinations, we modeled synthetic age distributions by mixing the source terranes and then iteratively calculating the synthetic age distribution that gave the minimum mismatch to the observed age distribution for a given stratum (Fig. 12). The Kolmogorov-Smirnov test returned high *P* values (>0.99) for the best-fit samples and indicates that the observed and synthetic age distributions are statistically indistinguishable.

Modeling of the detrital zircon age distributions from Hualong basin strata quantifies a significant provenance change after 22.5 Ma (Fig. 12A). Age distributions from 28, 24.5, and 22.5 Ma Hualong strata are statistically indistinguishable (Kolmogorov-Smirnov *P* > 0.08, 80 m.y. smoothing window) and are dominated by ~75% zircons derived from the two West Qinling units: Triassic plutonic (Tp) and Triassic flysch (Tr). A striking provenance change by 19 Ma is highlighted by the doubling of zircons derived from the two Laji-Jishi Shan units— Paleozoic (Pp and Cv) and Silurian (S)—to ~50% of the distribution (Fig. 12A). This strengthening of the Laji-Jishi Shan as a source area for Xunhua Basin is sustained throughout the upper Hualong section, with samples from 19, 13.5, and 10 Ma strata being statistically identical (Kolmogorov-Smirnov *P* > 0.44, 80 m.y. smoothing window). The enhanced contribution from the Laji-Jishi Shan starting between

Figure 12. Source-terrane mixtures (Fig. 11A) that best match zircon-age distributions (Figs. 11B and 11C) from selected magnetostratigraphic horizons from Xunhua (A) and Linxia (B) Basins. Mixtures were determined from our four-component sediment-mixing model (Amidon et al., 2005; Lease et al., 2007), run with a smoothing window of 80 m.y. Note intensified erosion of the Laji Shan expressed in Hualong (Xunhua) strata after 22.5 Ma and intensified erosion of the Jishi Shan expressed in Linxia strata after 14.5 Ma. WJS—Wangjiashan section.
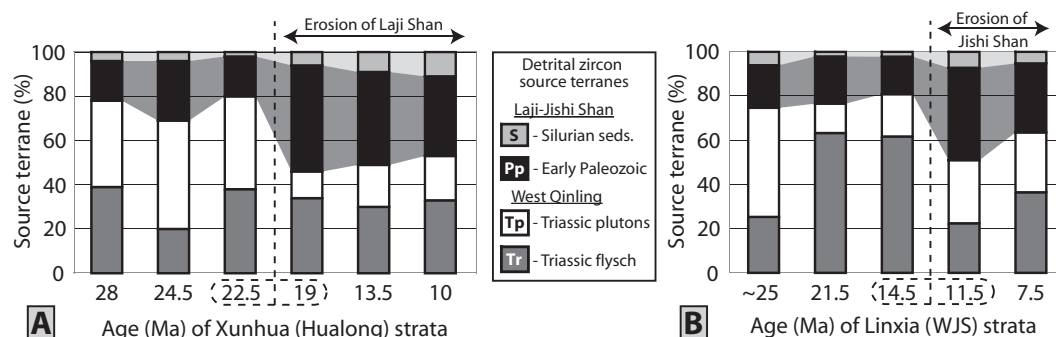
22.5 and 19 Ma indicates that the Paleozoic and Silurian source terranes in the Laji Shan were exposed and actively eroding by ca. 20 Ma. We attribute this exposure to accelerated rock uplift in the Laji Shan at or before this time.

Detrital zircon age distributions (Fig. 11C) from the Wangjiashan magneto- and lithostratigraphic section in western Linxia Basin (Fang et al., 2003; Fig. 1B) show a major provenance change after 14.5 Ma, with an abrupt doubling of Laji-Jishi Shan zircons by 11.5 Ma (Fig. 12B). Age distributions for the 25, 21.5, and 14.5 Ma Linxia strata are each dominated by ~75% zircons from the two West Qinling units—Triassic plutonic (Tp) and Triassic flysch (Tr)—with only a minor 25% of zircons from the Laji-Jishi Shan units. A striking provenance change by 11.5 Ma is highlighted by the doubling of zircons derived from the Laji-Jishi Shan units: Paleozoic (Pp and Cv) and Silurian (S). This strengthening of the Laji-Jishi Shan as a source area for Linxia Basin is sustained throughout the upper Wangjiashan section, where the 7.5-Ma stratum have ~40% Laji-Jishi Shan–derived zircons. We interpret the abrupt increase in Laji-Jishi Shan–derived zircons between 14.5 and 11.5 Ma to indicate that basement terranes in the nearby Jishi Shan became a dominant sediment source for the Linxia Basin at this time.

DISCUSSION

The Hualong magnetostratigraphy provides a late Oligocene–late Miocene record having better accuracy and higher resolution than contemporaneous records from nearby basins. The Hualong magnetostratigraphy, with its in situ *Hipparion weihoense* fossil, provides a rather convincing correlation to the GPTS between 9.5 Ma and 25 Ma, with 55 chronostratigraphic tie points overlying a more uncertain chronology between 25 Ma and 30 Ma (Fig. 7). Nearby magnetostratigraphy from Linxia Basin, on the other hand, has a more ambiguous correlation to the

GPTS between 2 and 29 Ma (Fang et al., 2003; Li et al., 1997). Furthermore, discrepancies between fossil ages and magnetostratigraphy in Linxia have caused some vertebrate paleontologists to suggest errors as great as 4–8 m.y. in the late Oligocene–Miocene portion of the Linxia magnetostratigraphic correlation (Deng et al., 2004; Garzione et al., 2005). Regardless of the details, Linxia Basin does contain an invaluable late Cenozoic stratigraphic record that has served as a useful time line for continental climatic records (Dettman et al., 2003; Fan et al., 2007, 2006; Garzione et al., 2005; Wang and Deng, 2005). The Hualong section in northern Xunhua Basin, however, provides a contemporaneous record where sub-million-year Miocene stratigraphic age constraints are known with greater fidelity than in Linxia. Consequently, we exploit the high-resolution Hualong magnetostratigraphic record to interpret variations in sediment accumulation along the northeastern Tibetan Plateau margin in the context of local range growth (Fig. 9). Relative climatic quiescence throughout the late Oligocene–early Miocene (Dettman et al., 2003) suggests that regional climate change alone did not induce the changes in subsidence rates and source areas that we detect in the magnetostratigraphic record. Furthermore, if climate were the dominant control on deposition, then a shift to more arid conditions in this region starting in middle Miocene time (Dettman et al., 2003; Garzione et al., 2005; Kent-Corson et al., 2009) should have led to a decrease in erosion and deposition rates, rather than the increase that we find.

Our integration of detrital zircon records of provenance within magnetostratigraphic sections distinguishes this study from most others. Detrital zircon ages allow us to distinguish sediment sources in the plateau interior to the south from sources outboard of the plateau margin to the north—areas with somewhat similar gross bedrock lithologies, though each area has a unique zircon U/Pb age spectrum (Fig. 10). Our

determination of zircon age distributions from specific strata of known age within the Xunhua and Linxia Basin magnetostratigraphies allows us to track the evolution of plateau margin sources and thus tectonism throughout the late Oligocene–Miocene (Figs. 13 and 14).

Additionally, the Xunhua Basin lies at a crossroads between studied sections in Linxia, Xining, and Guide Basins (Fig. 1B), and consequently analysis of Xunhua deposition illuminates broader, regional depositional patterns. Our detailed Xunhua magnetostratigraphic (Fig. 7), sedimentologic (Fig. 2), and subsidence (Fig. 9) analyses, when compared to adjacent records, clearly define significant lateral variations in both depositional environments (Figs. 13 and 14) and accumulation rates (Fig. 15) in this region of Tibet. Furthermore, detrital zircon provenance records from Xunhua and Linxia Basin stratigraphy document changes in source terranes that can be tied to newly emergent ranges (Fig. 12). Collectively, these analyses suggest that Xunhua Basin has been adjacent to emerging high terrain in the Laji Shan since ca. 22 Ma and Jishi Shan since ca. 13 Ma. The erosion of these ranges at ca. 22 Ma and ca. 13 Ma is also corroborated by vertical transects of low-temperature thermochronometer ages from the hanging walls of the range-bounding thrust faults (Lease et al., 2011).

Growth of the Laji Shan ca. 22 Ma

Growth of the Laji Shan at ca. 22 Ma is expressed in northern Xunhua Basin by a pulse of enhanced sediment accumulation, changes in detrital zircon provenance, and coarsening-upward facies. The Hualong magnetostratigraphic record shows a distinct period of rapid sediment accumulation and basin subsidence rates during 24–21 Ma (Fig. 9). Peak accumulation rates during the 24–22.5 Ma interval are more than two times higher than rates during the subsequent 21–12 Ma period; peak subsidence
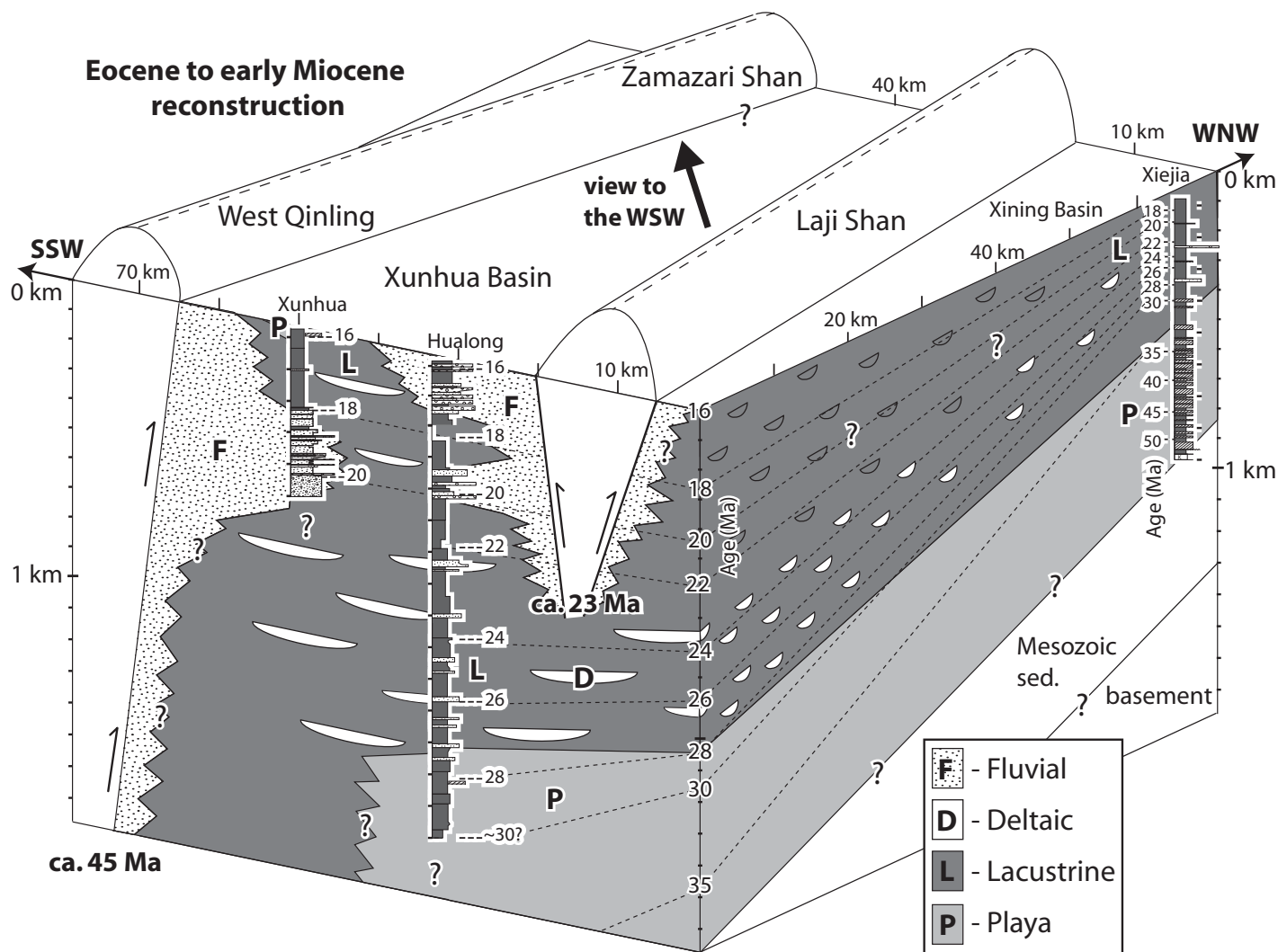
Figure 13. Eocene to early Miocene block diagram reconstruction synthesizing differences in sediment thickness, age, depositional facies, and provenance relationships among magnetostratigraphic sections with >16 Ma strata in Xunhua (this paper; Hough et al., 2011) and Xining (Dai et al., 2006; Dupont-Nivet et al., 2007) Basins. Location is shown in Figure 1B.

rates are 3–4 times higher. Rapid tectonic subsidence until ca. 21 Ma suggests enhanced flexural loading by thrust-thickened crust until this time. This period of accelerated subsidence is corroborated by low-temperature thermochronology from the hanging wall of the eastern Laji Shan thrust fault, which shows the onset of rapid cooling at ca. 22 Ma after an extended period of slow cooling since the Late Cretaceous (Lease et al., 2011). We interpret that enhanced flexural loading evinced by the rapid tectonic subsidence in Hualong is a response to growth of the Laji Shan.

The change in Hualong depositional environment from prolonged marginal lacustrine/deltaic plain deposition (unit 1; 30–20 Ma) to alluvial-fan deposition (unit 2) at 20 Ma and then to braided fluvial deposition (unit 3) by

17.5 Ma (Figs. 3 and 9) suggests an influx of coarse sediment from an emergent or encroaching source area. Provenance determinations from 22.5 Ma and 19 Ma strata (Fig. 12A) show that the coarsening-upward facies transition is accompanied by a change to enhanced erosion of detritus unique to basement terranes in the Laji-Jishi Shan and further supports the interpretation that this range became a significant source area at this time. Unfortunately, we cannot discriminate Laji Shan versus Jishi Shan source terranes with detrital zircon ages because, within the resolution of our data, these two ranges have identical age signatures. Additionally, a preliminary examination of Laji Shan versus Jishi Shan zircon grains show that zircons from the two ranges have similar, non-unique rare earth element patterns.

Several independent lines of evidence, however, suggest that the change in detrital zircon signature recorded in Hualong by 19 Ma can be reliably attributed to growth of the Laji Shan. First, the similarity of oxygen isotopic values between Xunhua Basin and Linxia Basin sediments between 20 and 16 Ma (Hough et al., 2011) suggests that the two basins were linked during this time with a nonextant or subdued Jishi Shan. Second, thermochronology indicates rapid erosion of the Laji Shan, but not the Jishi Shan, in the early Miocene (Lease et al., 2011). Third, paleocurrents from our oldest site at 17.5 Ma until 13.5 Ma show a range of southerly paleoflow directions that are consistent with flow away from the Laji Shan (Fig. 3). Thus, the change in zircon signature recorded in Hualong by 19 Ma is most reasonably attributed to a
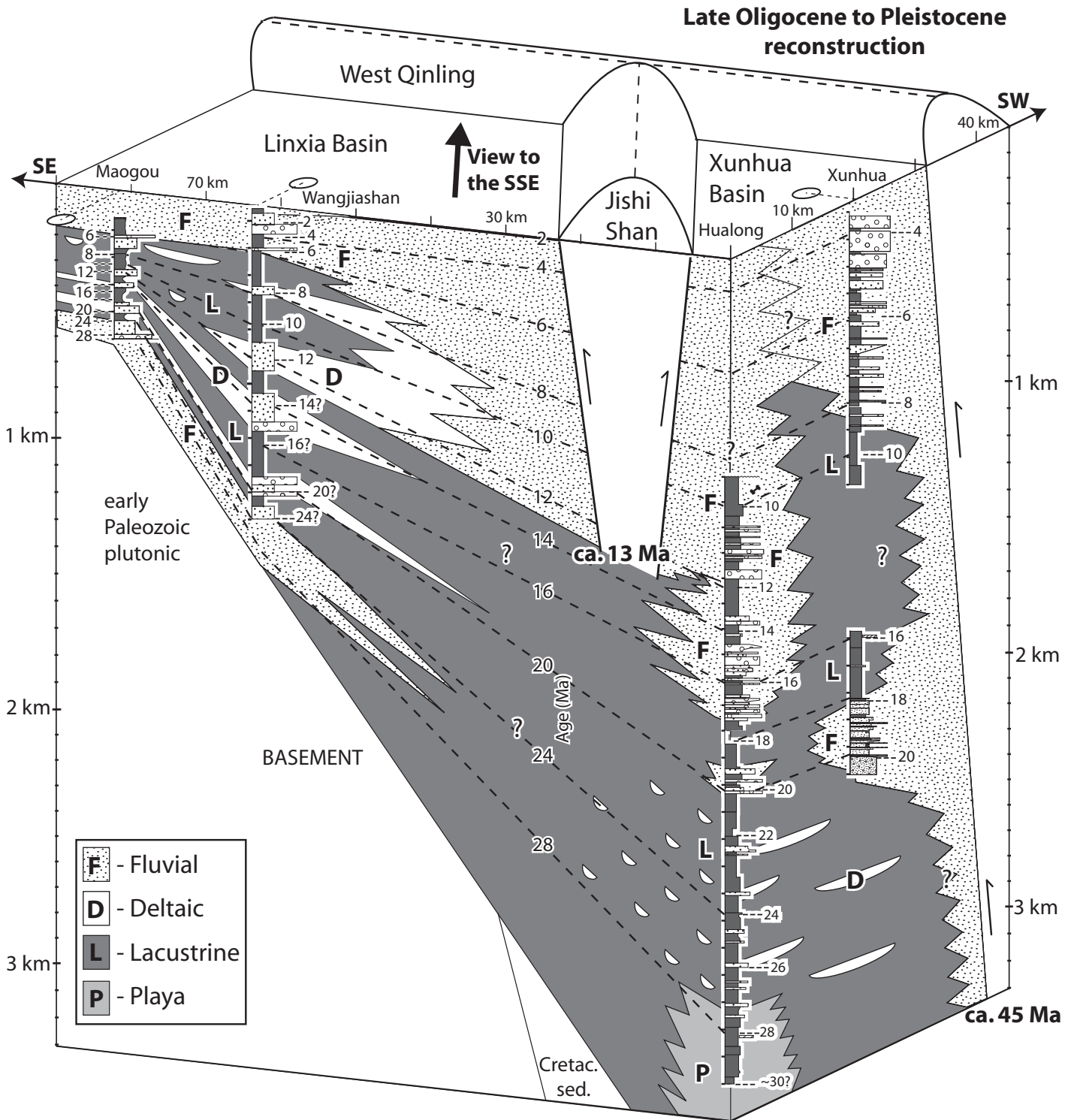
Figure 14. Late Oligocene to Pleistocene block diagram reconstruction synthesizing differences in sediment thickness, age, depositional facies, and provenance relationships among magnetostratigraphic sections in Xunhua Basin (this paper; Hough et al., 2011) and magneto- and lithostratigraphic sections in Linxia Basin (Fan et al., 2006; Fang et al., 2003; Li et al., 1997). Location shown in Figure 1B.

Figure 15. (A) Maps of sediment accumulation rates at 5 m.y. intervals from magnetostratigraphic sections in Xunhua and adjacent basins (Dai et al., 2006; Fang et al., 2003, 2005; Hough et al., 2011). (B) Age versus compacted thickness for sections in Xunhua and adjacent basins shown in A. Black lines in background denote linear regressions for each section at 5 m.y. intervals.
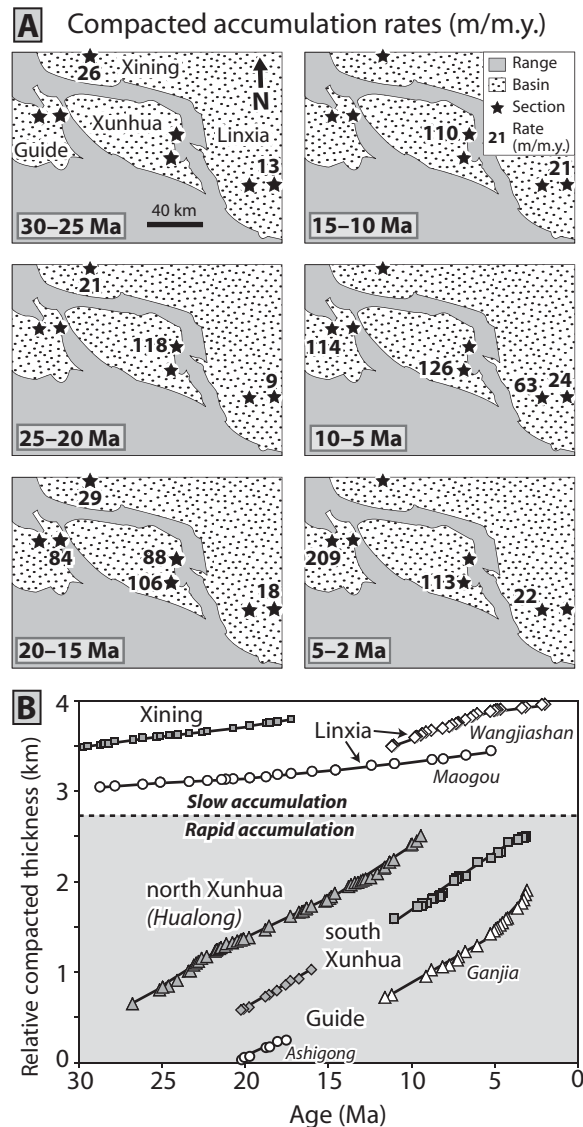
uncertain whether the 12 Ma acceleration in Hualong sediment accumulation was due to an increase in sediment supply, accommodation space, or ponding behind the emergent Jishi Shan, each of these scenarios is consistent with growth of the Jishi Shan at this time. Finally, growth of the Jishi Shan at ca. 13 Ma is consistent with local climate records from calcareous basin fills that show divergence of Linxia and Xunhua oxygen isotopic values; this result signals topographic isolation of these two basins by surface uplift of the intervening Jishi Shan by 11 Ma (Hough et al., 2011).

Regional Depositional Environments, Provenance, and Accumulation Patterns

The late Oligocene depositional history of the northern Xunhua Basin and the Xining Basin to the northwest was characterized by a prolonged period of marginal lacustrine, playa, and deltaic plain deposition (Fig. 13). Widespread playa facies extend as far back as the early Eocene in the Xining Basin (Dai et al., 2006; Dupont-Nivet et al., 2007). The abundance of evaporitic facies suggests a semiarid environment. Detrital zircon age distributions from Upper Oligocene deposits are dominated by 70%–80% West Qinling zircons in both Xunhua and Linxia deposits (Fig. 12) and indicate that sediment was derived primarily from southern sources in the plateau interior. Marginal lacustrine deposition continued until 20 Ma in the northern Xunhua Basin, when it was terminated by a pulse of coarse alluvial deposition (Fig. 13). Detrital zircon age distributions from these Xunhua alluvial deposits show a notable change in source areas, and, for the first time, they contain >50% Laji-Jishi Shan zircons, thereby indicating a significant sediment source north of the West Qinling (Fig. 12).

Chronostratigraphic analysis of Miocene deposits from two magnetostratigraphic sections within the Xunhua Basin that are separated by ~20 km along a north-south transect (Fig. 1B) defines a depositional environment where (1) in the early Miocene, the northern and southern parts of Xunhua Basin received alluvial sediment of different origin (Fig. 13), and (2) in the middle and late Miocene, fluvial deposits in the north graded into a lacustrine environment toward the south (Fig. 14). Although alluvial deposits occur from 20 Ma until 18 or 19 Ma in both the northern Xunhua (Hualong) section and the southern Xunhua section (Hough et al., 2011), these alluvial deposits are of different depositional character and were sourced from different ranges. Immature, coarse alluvial-fan deposits in Hualong (Fig. 2) were deposited during the same interval as more mature, finer-grained fluvial sediments in the southern

Laji Shan bedrock source near the area of rapid erosion revealed by low-temperature thermochronology. Finally, regional patterns of accumulation and depositional facies suggest that the Xunhua Basin was an important early Miocene depocenter (discussed later herein, under Regional Depositional Environments, Provenance, and Accumulation Patterns).

Growth of the Jishi Shan ca. 13 Ma

Detailed analyses of magnetostratigraphy and provenance from basins flanking both sides of the Jishi Shan reveal the emergence of this range at ca. 13 Ma and corroborate thermochronological and climatic records. Based on synthesis of results described here for the eastern side of the range, an up-section change in Linxia Basin detrital zircon signatures between

14.5 and 11.5 Ma brackets the emergence of the Laji-Jishi Shan as an active sediment source for Linxia Basin (Fig. 12B). We ascribe this change to enhanced erosion of the Jishi Shan (not the Laji Shan), in part because apatite (U-Th)/He and fission-track age-elevation data from the Jishi Shan thrust hanging wall show the onset of accelerated uplift and erosion of the range at ca. 13 Ma (Lease et al., 2011).

On the western side of the Jishi Shan in Xunhua Basin, magnetostratigraphic records from the Hualong basin show two notable changes at 12 Ma that we ascribe to uplift of the Jishi Shan: (1) a 50% acceleration in sediment accumulation rate at the top of the section (12–9 Ma; Fig. 9) and (2) consistently westward paleocurrents throughout this interval in Hualong (Fig. 3), which suggest sediment being shed from the emergent Jishi Shan to the east. Although it is

Xunhua basin (Hough et al., 2011). Furthermore, whereas post–20 Ma Hualong deposits contain detrital zircons showing a dominant Laji-Jishi Shan source (Fig. 12A), southern Xunhua conglomerates are dominated by clasts from the West Qinling (Hough et al., 2011). After 18 Ma, the southern Xunhua Basin transitioned to a lacustrine to marginal lacustrine environment with magnetostratigraphic records at 18–15.8 Ma and 11–8.75 Ma (Hough et al., 2011) (Figs. 13 and 14). In the northern Xunhua Basin, on the other hand, fluvial deposition continued uninterrupted from 18 Ma until the top of the section at 9 Ma. This southward-fining lateral facies variation from coarse fluvial facies in the northern Xunhua Basin to finer lacustrine facies in the southern Xunhua Basin also suggests the emergence of the Laji Shan to the north as an important source area.

Until middle Miocene time, the Xunhua and Linxia Basins appear to have shared a hydrological connection (Hough et al., 2011), although Xunhua received 3–8 times thicker accumulation of late Oligocene–middle Miocene sediment than Linxia (Fig. 14). Average $\delta^{18}O$ isotopic compositions within calcareous basin fills are similar, suggesting that the Xunhua and Linxia Basins were hydrologically linked until 11–16 Ma (Hough et al., 2011). Average early and middle Miocene accumulation rates in the Xunhua Basin, however, were 5–13 times higher than contemporaneous rates in the Linxia Basin to the east and 3–6 times higher than rates in the Xining Basin to the west (Fig. 15). The significantly greater magnitude and rates of accumulation in Xunhua Basin suggest that it was an important depocenter lying near a potential locus of crustal flexure in the Laji Shan. Furthermore, westward paleoflow within the ca. 20 Ma and ca. 14 Ma deltaic units in the Wangjiashan section in western Linxia Basin (Garzione et al., 2005) suggest flow toward a Xunhua depocenter in the west (Fig. 14).

Uplift of the Jishi Shan at ca. 13 Ma (Lease et al., 2011) disrupted the hydrological connection between the Xunhua and Linxia Basins (Hough et al., 2011), and, accordingly, late Miocene sedimentation in these basins likely responded to different controls. Jishi Shan uplift was the last in a series of range-growth events that collectively isolated Xunhua from surrounding areas and promoted intermontane ponding of sediment. The onset of uplift at ca. 13 Ma in the Jishi Shan, ca. 22 Ma in the Laji Shan (Lease et al., 2011), and ca. 45–50 Ma in the West Qinling (Clark et al., 2010) defined the eastern, northern, and southwestern margins of Xunhua Basin, respectively. In Linxia Basin, on the other hand, subsidence rates that increase with time are interpreted to indicate that flexural

subsidence continued until ca. 6 Ma (Fang et al., 2003). Additionally, a threefold gradient in late Miocene accumulation rates in Linxia Basin from two magnetostratigraphic sections (Fang et al., 2003) along an ~20 km transect orthogonal to the Jishi Shan (Fig. 15) suggests a strong flexural control on local deposition.

Subsidence versus Supply

Models of foreland basins suggest that grain-size changes and subsidence rates depend on whether deposition is driven by subsidence or supply (e.g., Flemings and Jordan, 1989; Heller and Paola, 1992; Heller et al., 1988; Paola et al., 1992). Progradation of coarse-grained facies in a supply-driven basin should coincide with relatively fast subsidence and sediment accumulation rates. Progradation of coarse-grained facies in a subsidence-driven basin, however, is inhibited during periods of relatively fast subsidence rates and instead coincides with relatively slow subsidence and sediment accumulation rates.

The Hualong stratigraphic record suggests subsidence-driven foreland deposition, where the period of most rapid subsidence and accumulation (27–21 Ma; Figs. 9A, 9B, and 9C) corresponds to the deposition of the fine-grained muds of unit 1 (Fig. 9D). Furthermore, the period of slowest subsidence and accumulation (21–12 Ma) corresponds to the deposition of coarse-grained conglomerates and sandstones of units 2 and 3 (Fig. 9). Although the Hualong magnetostratigraphic section only provides a one-dimensional record, the synchrony of coarse-grained deposition with the slowest subsidence and accumulation rates suggests that progradation of gravel across the northern Xunhua Basin did not occur until after local flexural loading (i.e., tectonically driven subsidence) diminished significantly in magnitude after 21 Ma. This finding is consistent with a subsidence-driven setting modulated by thrust loading of the Laji Shan to the north.

Additionally, the considerably greater thicknesses and rates of late Oligocene–middle Miocene accumulation in Xunhua relative to Linxia and Xining indicate significant subsidence adjacent to the eastern Laji Shan (Figs. 13 and 14). Late Oligocene–middle Miocene accumulation rates in Hualong were 3–13 times more rapid than contemporaneous rates in Linxia and Xining (Fig. 15). Between 28 and 20 Ma, relatively rapid accumulation of fine-grained lacustrine muds in Hualong (~120 m/m.y.) occurred at the same time as relatively slow accumulation of coarser-grained fluvial and deltaic facies in Linxia (~10 m/m.y.) (Figs. 13 and 14). The regional correlation of fine-grained deposits with the most rapid accumulation rates suggests that

subsidence rather than supply was the dominant control on sediment accumulation rates in the late Oligocene to middle Miocene Xunhua-Linxia foreland.

Regional Tectonic Implications

Recognition of the erosion and topographic development of the Laji Shan at ca. 22 Ma illuminates a poorly known episode of the Cenozoic geological history of the northeastern Tibetan Plateau. The West Qinling defined the northeastern plateau margin by 45–50 Ma, within a few million years after initial India-Asia continental collision, with the implication that stresses were transmitted instantaneously (from a geological perspective) over very large (>3000 km) distances (Clark et al., 2010; Dayem et al., 2009). Over the next 25 million years, the deformation front on the northeastern plateau margin was apparently stationary until it jumped northward ~60 km with pulsed growth of the Laji Shan at ca. 22 Ma.

Observations from bedrock cooling in bounding ranges and basin subsidence suggest that slip on the Laji Shan fault was pulsed and decelerated after ca. 18 Ma. Modeling of Laji Shan thermochronological data indicates an order-of-magnitude slowdown in cooling by 15–18 Ma (Lease et al., 2011), and subsidence records adjacent to the Laji Shan in northern Xunhua Basin show a three- to fourfold decrease in subsidence rates after 21 Ma (Fig. 9). On the West Qinling fault ~60 km to the south, on the other hand, Clark et al. (2010) interpreted a coeval period of accelerated faulting; this interpretation is based on thermochronological data that suggest a twofold increase in erosion rates beginning at ca. 18 Ma. We speculate that these observations together suggest transfer of fault slip from the Laji Shan to the West Qinling and out-of-sequence rejuvenation of thrusting in the West Qinling. The relatively low-lying area between the West Qinling and Laji Shan ranges that is occupied by the Xunhua Basin is devoid of any notable structures accommodating north-south contraction (Figs. 2, 13, and 14). This paucity of structures suggests that the Xunhua Basin area has not been thickened via distributed north-south shortening across the basin in Oligocene-to-Holocene time, but instead that deformation has been persistently localized across either the Laji Shan or West Qinling.

The development of the north-trending Jishi Shan at ca. 13 Ma is significant because this range is oriented obliquely to and developed later than both the WNW-trending Laji Shan (ca. 22 Ma) and the NW-trending West Qinling (ca. 45–50 Ma; Clark et al., 2010) nearby. Temporal variations in the orientation of Cenozoic

range growth have been interpreted to reflect a middle Miocene reorganization of deformation, from primarily NNE-SSW contraction, which mimics the plate convergence direction, to the inclusion of east-west motion (Lease et al., 2011). One expected consequence of such a reorganization—left-lateral strike-slip motion on the West Qinling and Laji Shan faults—has been documented in Quaternary time (Li, 2005; Yuan et al., 2005). Furthermore, the present geodetic field in this area, which is dominated by N110°E motion oriented orthogonally to the Jishi Shan (Duvall and Clark, 2010; Gan et al., 2007), suggests that this interpretation is plausible. Detailed structural and kinematic analyses of range-bounding faults, however, await further investigation. The onset of accelerated exhumation on north-trending structures in both the Jishi Shan (ca. 13 Ma) and nearby Liupan Shan (ca. 8 Ma), ~320 km to the east (Zheng et al., 2006), may signal the start of the modern deformation regime in northeastern Tibet, where contraction is coupled to left-lateral strike-slip motion in a complex regional stepover between the Kunlun and Haiyuan left-lateral faults (Duvall and Clark, 2010). Widespread middle and late Miocene accelerations in faulting, erosion, and deposition, as well as coarsening-upward facies and climatic records suggest intensified tectonic activity and changing kinematics in northeastern Tibet since this time (see Fig. 1A, and references therein; Kent-Corson et al., 2009; Molnar, 2005; Ritts et al., 2008; Wang et al., 2011b).

CONCLUSION

Sedimentary successions from the northern Xunhua Basin provide a unique view of the late Oligocene–Miocene history of northeastern Tibet because these archives are particularly sensitive to small increments of growth of nearby ranges that more distant basins fail to clearly record. The Hualong section displays a more than twofold acceleration in sediment accumulation and basin subsidence during 24–21 Ma and a transition to alluvial facies at 20 Ma that was coincident with intensified erosion of basement source terranes in the Laji-Jishi Shan by 19 Ma. Together, these findings suggest growth of the Laji Shan at 24–21 Ma in a subsidence-driven setting where progradation of coarse facies was inhibited during the period of most intense subsidence. Additionally, bedrock thermochronology suggests the onset of rapid Laji Shan cooling at ca. 22 Ma. Furthermore, an analysis of regional patterns of depositional facies and accumulation rates indicates that the Xunhua Basin was an important early Miocene depocenter that lay along the southern margin of the Laji Shan.

Later growth of the Jishi Shan after ca. 13 Ma accommodated east-west contraction. Enhanced erosion of the Jishi Shan is indicated by a change in the detrital zircon signature of Linxia Basin sediments by 11.5 Ma and by an acceleration in sediment accumulation in Hualong Basin starting at 12 Ma. Furthermore, the divergence of oxygen isotopic ratios between southern Xunhua and Linxia Basin strata by 11 Ma suggests topographic development of the intervening Jishi Shan and the growing presence of a rain shadow. Finally, bedrock thermochronology suggests the onset of rapid cooling and thrust-induced erosion in the Jishi Shan at ca. 13 Ma.

The history of the Tibetan Plateau between 40 and 13 Ma is characterized by relatively small magnitudes of range growth along the plateau's northeastern margin. The northeastern limit of plateau deformation in this area, established in the early Eocene shortly after initial India-Asia continental collision (Clark et al., 2010), remained largely stationary over the next 25 m.y. and only jumped 60 km to the north in early Miocene time with pulsed uplift of the Laji Shan. Growth of the north-trending Jishi Shan and Liupan Shan beginning ~10 m.y. later suggests that this sector of the plateau was accommodating east-west motion by middle Miocene time.

REFERENCES CITED

Abels, H.A., Dupont-Nivet, G., Xiao, G., Bosboom, R.E., and Krijgsman, W., 2011, Step-wise change of Asian interior climate preceding the Eocene-Oligocene transition (EOT): Palaeogeography, Palaeoclimatology, Palaeoecology, v. 299, no. 3–4, p. 399–412, doi:10.1016/j.palaeo.2010.11.028.

Allen, P.A., and Allen, J.R., 2005, Basin Analysis: Principles and Applications: Oxford, UK, Wiley-Blackwell, 560 p.

Amidon, W.H., Burbank, D.W., and Gehrels, G.E., 2005, U-Pb zircon ages as a sediment mixing tracer in the Nepal Himalaya: Earth and Planetary Science Letters, v. 235, no. 1–2, p. 244–260, doi:10.1016/j.epsl.2005.03.019.

Besse, J., and Courtillot, V., 2002, Apparent and true polar wander and the geometry of the geomagnetic field over the last 200 Myr: Journal of Geophysical Re-

search–Solid Earth, v. 107, no. B11, 2300, doi:10.1029/2000JB000050.

Blair, T.C., and McPherson, J.G., 1992, The Trollheim alluvial fan and facies model revisited: Geological Society of America Bulletin, v. 104, no. 6, p. 762–769, doi:10.1130/0016-7606(1992)104<0762:TTAFAF>2.3.CO;2.

Bovet, P.M., Ritts, B.D., Gehrels, G., Abbink, A.O., Darby, B., and Hourigan, J., 2009, Evidence of Miocene crustal shortening in the North Qilian Shan from Cenozoic stratigraphy of the western Hexi Corridor, Gansu Province, China: American Journal of Science, v. 309, no. 4, p. 290–329, doi:10.2475/00.4009.02.

Cabrera, L., Colombo, F., and Robles, S., 1985, Sedimentation and tectonic interrelationships in the Paleogene marginal alluvial systems of the SE Ebro basin. Transition from alluvial to shallow lacustrine environments, *in* Milá, M., and Rosell, J., eds., Excursion guidebook of the 6th European Regional IAS meeting (Lleida, Spain): Barcelona, International Association of Sedimentologists and Institut d'Estudis Ilerdencs, Universitat Autònoma de Barcelona, p. 393–492.

Cande, S.C., and Kent, D.V., 1995, Revised calibration of the geomagnetic polarity time scale for the Late Cretaceous and Cenozoic: Journal of Geophysical Research, v. 100, p. 6093–6095, doi:10.1029/94JB03098.

Cardozo, N., 2009, OSXBackstrip v2.6: http://homepage.mac.com/nfcd/work/programs.html (last accessed July 2009).

Clark, M.K., House, M.A., Royden, L.H., Whipple, K.X., Burchfiel, B.C., Zhang, X., and Tang, W., 2005, Late Cenozoic uplift of southeastern Tibet: Geology, v. 33, no. 6, p. 525–528, doi:10.1130/ G21265.1.

Clark, M.K., Farley, K.A., Zheng, D., Wang, Z.C., and Duvall, A., 2010, Early Cenozoic faulting on the northern Tibetan Plateau margin from apatite (U-Th)/He ages: Earth and Planetary Science Letters, v. 296, no. 1–2, p. 78–88, doi:10.1016/j.epsl.2010.04.051.

Collinson, J.D., 1996, Alluvial sediments, *in* Reading, H.G., ed., Sedimentary Environments: Processes, Facies, and Stratigraphy: Oxford, UK, Blackwell Publishing, Inc., p. 37–82.

Craddock, W.H., Kirby, E., Harkins, N.W., Zhang, H.P., Shi, X.H., and Liu, J.H., 2010, Rapid fluvial incision along the Yellow River during headward basin integration: Nature Geoscience, v. 3, no. 3, p. 209–213, doi:10.1038/ngeo777.

Craddock, W.H., Kirby, E., and Zheng, D.W., 2011, Late Miocene-Pliocene range growth in the interior of the northeastern Tibetan Plateau: Lithosphere, v. 3, no. 6, p. 420–438, doi:10.1130/L159.1.

Dai, S., Fang, X.M., Dupont-Nivet, G., Song, C.H., Gao, J.P., Krijgsman, W., Langereis, C., and Zhang, W.L., 2006, Magnetostratigraphy of Cenozoic sediments from the Xining Basin: Tectonic implications for the northeastern Tibetan Plateau: Journal of Geophysical Research–Solid Earth, v. 111, B11102, doi:10.1029/2005JB004187.

Dayem, K.E., Molnar, P., Clark, M.K., and Houseman, G.A., 2009, Far-field lithospheric deformation in Tibet during continental collision: Tectonics, v. 28, TC6005, doi:10.1029/2008TC002344.

DeCelles, P.G., Gray, M.B., Cole, R.B., Pequera, N., Pivnik, D.A., Ridgway, K.D., and Srivastava, P., 1991, Controls on synorogenic alluvial-fan architecture, Beartooth Conglomerate: Wyoming and Montana: Sedimentology, v. 38, p. 567–590, doi:10.1111/j.1365-3091.1991.tb01009.x.

DeCelles, P.G., Gehrels, G.E., Najman, Y., Martin, A.J., Carter, A., and Garzanti, E., 2004, Detrital geochronology and geochemistry of Cretaceous–early Miocene strata of Nepal: Implications for timing and diachroneity of initial Himalayan orogenesis: Earth and Planetary Science Letters, v. 227, no. 3–4, p. 313–330, doi:10.1016/j.epsl.2004.08.019.

DeGraaff-Surpless, K., Mahoney, J.B., Wooden, J.L., and McWilliams, M.O., 2003, Lithofacies control in detrital zircon provenance studies: Insights from the Cretaceous Methow basin, southern Canadian Cordillera: Geological Society of America Bulletin, v. 115, no. 8, p. 899–915, doi:10.1130/B25267.1.

Deng, T., Wang, X., Ni, X.J., and Liu, L., 2004, Sequence of Cenozoic mammalian faunas of the Linxia Basin in

Gansu, China: Acta Geologica Sinica, v. 78, no. 1, p. 8–14.

Dettman, D.L., Fang, X.M., Garzione, C.N., and Li, J.J., 2003, Uplift-driven climate change at 12 Ma: A long delta O-18 record from the NE margin of the Tibetan Plateau: Earth and Planetary Science Letters, v. 214, no. 1–2, p. 267–277, doi:10.1016/S0012-821X(03)00383-2.

Dupont-Nivet, G., Krijgsman, W., Langereis, C.G., Abels, H.A., Dai, S., and Fang, X.M., 2007, Tibetan Plateau aridification linked to global cooling at the Eocene-Oligocene transition: Nature, v. 445, no. 7128, p. 635–638, doi:10.1038/nature05516.

Dupont-Nivet, G., Dai, S., Fang, X., Krijgsman, W., Erens, V., Reitsma, M., and Langereis, C., 2008, Timing and distribution of tectonic rotations in the northeastern Tibetan Plateau, *in* Burchfiel, B.C., and Wang, E., eds., Investigations into the Tectonics of the Tibetan Plateau: Geological Society of America Special Paper 444, p. 73–87.

Duvall, A.R., and Clark, M.K., 2010, Dissipation of fast strike-slip faulting within and beyond northeastern Tibet: Geology, v. 38, no. 3, p. 223–226, doi:10.1130/G30711.1.

Duvall, A.R., Clark, M.K., van der Pluijm, B.A., and Li, C., 2011, Direct dating of Eocene reverse faulting in northeastern Tibet using Ar-dating of fault clays and low-temperature thermochronometry: Earth and Planetary Science Letters, v. 304, no. 3–4, p. 520–526, doi:10.1016/j.epsl.2011.02.028.

Enkelmann, E., Ratschbacher, L., Jonckheere, R., Nestler, R., Fleischer, M., Gloaguen, R., Hacker, B.R., Zhang, Y.Q., and Ma, Y.S., 2006, Cenozoic exhumation and deformation of northeastern Tibet and the Qinling: Is Tibetan lower crustal flow diverging around the Sichuan Basin?: Geological Society of America Bulletin, v. 118, no. 5–6, p. 651–671, doi:10.1130/B25805.1.

Fan, M.J., Dettman, D.L., Song, C.H., Fang, X.M., and Garzione, C.N., 2007, Climatic variation in the Linxia Basin, NE Tibetan Plateau, from 13.1 to 4.3 Ma: The stable isotope record: Palaeogeography, Palaeoclimatology, Palaeoecology, v. 247, no. 3–4, p. 313–328, doi:10.1016/j.palaeo.2006.11.001.

Fan, M.J., Song, C.H., Dettman, D.L., Fang, X.M., and Xu, X.H., 2006, Intensification of the Asian winter monsoon after 7.4 Ma: Grain-size evidence from the Linxia Basin, northeastern Tibetan Plateau, 13.1 Ma to 4.3 Ma: Earth and Planetary Science Letters, v. 248, no. 1–2, p. 186–197, doi:10.1016/j.epsl.2006.05.025.

Fang, X.M., Garzione, C., Van der Voo, R., Li, J.J., and Fan, M.J., 2003, Flexural subsidence by 29 Ma on the NE edge of Tibet from the magnetostratigraphy of Linxia Basin, China: Earth and Planetary Science Letters, v. 210, no. 3–4, p. 545–560, doi:10.1016/S0012-821X(03)00142-0.

Fang, X.M., Yan, M.D., Van der Voo, R., Rea, D.K., Song, C.H., Pares, J.M., Gao, J.P., Nie, J.S., and Dai, S., 2005, Late Cenozoic deformation and uplift of the NE Tibetan Plateau: Evidence from high-resolution magnetostratigraphy of the Guide Basin, Qinghai Province, China: Geological Society of America Bulletin, v. 117, no. 9–10, p. 1208–1225, doi:10.1130/B25727.1.

Flemings, P.B., and Jordan, T.E., 1989, A synthetic stratigraphic model of foreland basin development: Journal of Geophysical Research–Solid Earth, v. 94, no. B4, p. 3851–3866, doi:10.1029/JB094iB04p03851.

Friend, P.F., Slater, M.J., and Williams, R.C., 1979, Vertical and lateral building of river sandstone bodies, Ebro Basin, Spain: Journal of the Geological Society of London, v. 136, no. 1, p. 39, doi:10.1144/gsjgs.136.1.0039.

Gan, W.J., Zhang, P.Z., Shen, Z.K., Niu, Z.J., Wang, M., Wan, Y.G., Zhou, D.M., and Cheng, J., 2007, Present-day crustal motion within the Tibetan Plateau inferred from GPS measurements: Journal of Geophysical Research–Solid Earth, v. 112, B08416, doi:10.1029/2005JB004120.

Garzione, C.N., Ikari, M.J., and Basu, A.R., 2005, Source of Oligocene to Pliocene sedimentary rocks in the Linxia Basin in northeastern Tibet from Nd isotopes: Implications for tectonic forcing of climate: Geological Society of America Bulletin, v. 117, no. 9–10, p. 1156–1166, doi:10.1130/B25743.1.

Gehrels, G.E., Valencia, V., and Pullen, A., 2006, Detrital zircon geochronology by laser-ablation multicollector ICPMS at the Arizona Laserchron Center, *in* Olszewski, T., and Huff, W., eds., Geochronology: Emerging Opportunities: Philadelphia, Paleontological Society Short Course, p. 1–10.

Gilder, S., Chen, Y., Cogne, J.P., Tan, X.D., Courtillot, V., Sun, D.J., and Li, Y.G., 2003, Paleomagnetism of Upper Jurassic to Lower Cretaceous volcanic and sedimentary rocks from the western Tarim Basin and implications for inclination shallowing and absolute dating of the M-0 (ISEA?) chron: Earth and Planetary Science Letters, v. 206, no. 3–4, p. 587–600, doi:10.1016/S0012-821X(02)01074-9.

Godard, V., Pik, R., Lave, J., Cattin, R., Tibari, B., de Sigoyer, J., Pubellier, M., and Zhu, J., 2009, Late Cenozoic evolution of the central Longmen Shan, eastern Tibet: Insight from (U-Th)/He thermochronometry: Tectonics, v. 28, TC5009, doi:10.1029/2008TC002407.

Harkins, N., Kirby, E., Heimsath, A., Robinson, R., and Reiser, U., 2007, Transient fluvial incision in the headwaters of the Yellow River, northeastern Tibet, China: Journal of Geophysical Research–Earth Surface, v. 112, F03S04, doi:10.1029/2006JF000570.

Heller, P.L., and Paola, C., 1992, The large-scale dynamics of grain-size variation in alluvial basins: 2. Applications to syntectonic conglomerate: Basin Research, v. 4, p. 91–102, doi:10.1111/j.1365-2117.1992.tb00146.x.

Heller, P.L., Angevine, C.L., Winslow, N.S., and Paola, C., 1988, Two-phase stratigraphic model of foreland-basin sequences: Geology, v. 16, no. 6, p. 501–504, doi:10.1130/0091-7613(1988)016<0501:TPSMOF>2.3.CO;2.

Horton, B.K., Dupont-Nivet, G., Zhou, J., Waanders, G.L., Butler, R.F., and Wang, J., 2004, Mesozoic-Cenozoic evolution of the Xining-Minhe and Dangchang Basins, northeastern Tibetan Plateau: Magnetostratigraphic and biostratigraphic results: Journal of Geophysical Research–Solid Earth, v. 109, B04402, doi:10.1029/2003JB002913.

Hough, B.G., Garzione, C.N., Wang, Z.C., Lease, R.O., Burbank, D.W., and Yuan, D.Y., 2011, Stable isotope evidence for topographic growth and basin segmentation: Implications for the evolution of the NE Tibetan Plateau: Geological Society of America Bulletin, v. 123, no. 1–2, p. 168–185, doi:10.1130/B30090.1.

Johnson, N.M., and Mcgee, V.E., 1983, Magnetic polarity stratigraphy—Stochastic properties of data, sampling problems, and the evaluation of interpretations: Journal of Geophysical Research, v. 88, no. B2, p. 1213–1221, doi:10.1029/JB088iB02p01213.

Jones, C.H., 2002, User-driven integrated software lives: "Paleomag" paleomagnetics analysis on the Macintosh: Computers & Geosciences, v. 28, no. 10, p. 1145–1151, doi:Pii S0098–3004(02)00032–8.

Kent-Corson, M.L., Ritts, B.D., Zhuang, G.S., Bovet, P.M., Graham, S.A., and Chamberlain, C.P., 2009, Stable isotopic constraints on the tectonic, topographic, and climatic evolution of the northern margin of the Tibetan Plateau: Earth and Planetary Science Letters, v. 282, no. 1–4, p. 158–166, doi:10.1016/j.epsl.2009.03.011.

Kirby, E., Reiners, P.W., Krol, M.A., Whipple, K.X., Hodges, K.V., Farley, K.A., Tang, W.Q., and Chen, Z.L., 2002, Late Cenozoic evolution of the eastern margin of the Tibetan Plateau: Inferences from Ar-40/Ar-39 and (U-Th)/He thermochronology: Tectonics, v. 21, 1001, doi:10.1029/2000TC001246.

Kirschvink, J.L., 1980, The least-squares line and plane and the analysis of paleomagnetic data: Geophysical Journal of the Royal Astronomical Society, v. 62, no. 3, p. 699–718.

Kirschvink, J.L., Kopp, R.E., Raub, T.D., Baumgartner, C.T., and Holt, J.W., 2008, Rapid, precise, and high-sensitivity acquisition of paleomagnetic and rock-magnetic data: Development of a low-noise automatic sample changing system for superconducting rock magnetometers: Geochemistry, Geophysics, Geosystems, v. 9, Q05Y01, doi:10.1029/2007GC001856.

Lease, R.O., Burbank, D.W., Gehrels, G.E., Wang, Z.C., and Yuan, D.Y., 2007, Signatures of mountain building: Detrital zircon U/Pb ages from northeastern Tibet: Geology, v. 35, no. 3, p. 239–242, doi:10.1130/G23057A.1.

Lease, R.O., Burbank, D.W., Clark, M.K., Farley, K.A., Zheng, D., and Zhang, H., 2011, Middle Miocene reorganization of deformation along the northeastern Tibetan Plateau: Geology, v. 39, no. 4, p. 359–362, doi:10.1130/G31356.1.

Li, C., 2005, Quantitative research on several prominent faults in the NE margin of the Tibetan Plateau [Ph.D. thesis]: Bejing, China, Institute of Geology, China Earthquake Administration (in Chinese).

Li, J.J., Fang, X.M., Van der Voo, R., Zhu, J.J., Mac Niocaill, C., Cao, J.X., Zhong, W., Chen, H.L., Wang, J.L., Wang, J.M., and Zhang, Y.C., 1997, Late Cenozoic magnetostratigraphy (11–0 Ma) of the Dongshanding and Wangjiashan sections in the Longzhong Basin, western China: Geologie en Mijnbouw, v. 76, no. 1–2, p. 121–134, doi:10.1023/A:1003153717799.

Mack, G.H., James, W.C., and Monger, H.C., 1993, Classification of paleosols: Geological Society of America Bulletin, v. 105, no. 2, p. 129–136, doi:10.1130/0016-7606(1993)105<0129:COP>2.3.CO;2.

McFadden, P.L., and McElhinny, M.W., 1990, Classification of the reversal test in paleomagnetism: Geophysical Journal International, v. 103, no. 3, p. 725–729, doi:10.1111/j.1365-246X.1990.tb05683.x.

Métivier, F., Gaudemer, Y., Tapponnier, P., and Meyer, B., 1998, Northeastward growth of the Tibet Plateau deduced from balanced reconstruction of two depositional areas: The Qaidam and Hexi Corridor Basins, China: Tectonics, v. 17, no. 6, p. 823–842, doi:10.1029/98TC02764.

Miall, A.D., 1978, Lithofacies types and vertical profile models in braided river deposits: A summar, *in* Miall, A.D., ed., Fluvial Sedimentology: Memoirs of the Canadian Society of Petroleum Geologists, v. 5, p. 597–604.

Miall, A.D., 1996, The Geology of Fluvial Deposits: Sedimentary Facies, Basin Analysis, and Petroleum Geology: Berlin, New York, Springer, 582 p.

Molnar, P., 2005, Mio-Pliocene growth of the Tibetan Plateau and evolution of East Asian climate: Palaeontologia Electronica, v. 8, no. 1, p. 2A.

Molnar, P., and Stock, J.M., 2009, Slowing of India's convergence with Eurasia since 20 Ma and its implications for Tibetan mantle dynamics: Tectonics, v. 28, TC3001, doi:10.1029/2008TC002271.

Nanson, G.C., and Croke, J.C., 1992, A genetic classification of floodplains: Geomorphology, v. 4, no. 6, p. 459–486, doi:10.1016/0169-555X(92)90039-Q.

Nemec, W., and Steel, R.J., 1984, Alluvial and coastal conglomerates: Their significant features and some comments on gravelly mass-flow deposits, *in* Koster, E.H., and Steel, R.J., eds., Sedimentology of Gravels and Conglomerates: Calgary, Alberta, Canada, Canadian Society of Petroleum Geologists, p. 1–31.

Ogg, J.G., and Smith, A.G., 2004, The geomagnetic polarity time scale, *in* Gradstein, F.M., Ogg, J.G., and Smith, A., eds., Geological Time Scale: Cambridge, UK, Cambridge University Press, p. 65–86.

Ouimet, W., Whipple, K., Royden, L., Reiners, P., Hodges, K., and Pringle, M., 2010, Regional incision of the eastern margin of the Tibetan Plateau: Lithosphere, v. 2, no. 1, p. 50–63, doi:10.1130/L57.1.

Paola, C., Heller, P.L., and Angevine, C.L., 1992, The large-scale dynamics of grain-size variation in alluvial basins: 1. Theory: Basin Research, v. 4, p. 73–90, doi:10.1111/j.1365-2117.1992.tb00145.x.

Qinghai Bureau of Geology and Mineral Resources (QBGMR), 1991, Regional Geology of the Qinghai Province: Beijing, Geological Publishing House, 662 p.

Reading, H.G., and Collinson, J.D., 1996, Clastic coasts, *in* Reading, H.G., ed., Sedimentary Environments: Processes, Facies and Stratigraphy: Oxford, UK, Blackwell Publishing Inc., p. 154–231.

Ritts, B.D., Yue, Y.J., Graham, S.A., Sobel, E.R., Abbink, O.A., and Stockli, D., 2008, From sea level to high elevation in 15 million years: Uplift history of the northern Tibetan Plateau margin in the Altun Shan: American Journal of Science, v. 308, no. 5, p. 657–678, doi:10.2475/05.2008.01.

Schreiber, B.C., and El Tabakh, M., 2000, Deposition and early alteration of evaporites: Sedimentology, v. 47, p. 215–238, doi:10.1046/j.1365-3091.2000.00002.x.

Sclater, J.G., and Christie, P.A.F., 1980, Continental stretching—An explanation of the post-mid-Cretaceous subsidence of the central North Sea Basin: Journal of Geophysical Research, v. 85, no. B7, p. 3711–3739, doi:10.1029/JB085iB07p03711.

Talbot, M.R., and Allen, P.A., 1996, Lakes, *in* Reading, H.G., ed., Sedimentary Environments: Processes, Facies and Stratigraphy: Oxford, UK, Blackwell Publishing Inc., p. 83–124.

Tauxe, L., and Gallet, Y., 1991, A jackknife for magnetostratigraphy: Geophysical Research Letters, v. 18, no. 9, p. 1783–1786, doi:10.1029/91GL01223.

Tauxe, L.P., and Hartl, P., 1997, 11 million years of Oligocene geomagnetic field behavior: Geophysical Journal International, v. 128, p. 217–229, doi:10.1111/j.1365-246X.1997.tb04082.x.

Tauxe, L., and Watson, G.S., 1994, The fold test—An eigen analysis approach: Earth and Planetary Science Letters, v. 122, no. 3–4, p. 331–341, doi:10.1016/0012-821X(94)90006-X.

Tauxe, L., Butler, R.F., Banerjee, S.K., and Van der Voo, R., 2009, Essentials of Paleomagnetism: Berkeley, California, University of California Press, 512 p.

Wang, W.T., Zhang, P.Z., Kirby, E., Wang, L.H., Zhang, G.L., Zheng, D.W., and Chai, C.Z., 2011a, A revised chronology for Tertiary sedimentation in the Sikouzi Basin: Implications for the tectonic evolution of the northeastern corner of the Tibetan Plateau: Tectonophysics, v. 505, no. 1–4, p. 100–114, doi:10.1016/j.tecto.2011.04.006.

Wang, Y., and Deng, T., 2005, A 25 m.y. isotopic record of paleodiet and environmental change from fossil mammals and paleosols from the NE margin of the Tibetan Plateau: Earth and Planetary Science Letters, v. 236, no. 1–2, p. 322–338, doi:10.1016/j.epsl.2005.05.006.

Wang, Z.C., Zhang, P.Z., Garzione, C.N., Lease, R.O., Zhang, G., Zheng, D.W., Hough, B., Yuan, D.Y., Li, C., Liu, J., and Wu, Q., 2011b, Magnetostratigraphy and depositional history of the Miocene Wushan Basin on the NE Tibetan Plateau, China: Implications for middle Miocene tectonics of the West Qinling fault zone: Journal of Asian Earth Sciences (in press), doi:10.1016/j.jseaes.2011.06.009.

Yan, M., Van der Voo, R., Fang, X.-M., Pares, J.M., and Rea, D.K., 2006, Paleo-magnetic evidence for a mid-Miocene clockwise rotation of about 25° of the Guide Basin area in NE Tibet: Earth and Planetary Science Letters, v. 241, p. 234–247, doi:10.1016/j.epsl.2005.10.013.

Yin, A., and Harrison, T.M., 2000, Geologic evolution of the Himalayan-Tibetan orogen: Annual Review of Earth and Planetary Sciences, v. 28, p. 211–280, doi:10.1146/annurev.earth.28.1.211.

Yin, A., Rumelhart, P.E., Butler, R., Cowgill, E., Harrison, T.M., Foster, D.A., Ingersoll, R.V., Zhang, Q., Zhou, X.Q., Wang, X.F., Hanson, A., and Raza, A., 2002, Tectonic history of the Altyn Tagh fault system in northern Tibet inferred from Cenozoic sedimentation: Geological Society of America Bulletin, v. 114, no. 10, p. 1257–1295, doi:10.1130/0016-7606(2002)114<1257:THOTAT>2.0.CO;2.

Yin, A., Dang, Y.Q., Wang, L.C., Jiang, W.M., Zhou, S.P., Chen, X.H., Gehrels, G.E., and McRivette, M.W., 2008a, Cenozoic tectonic evolution of Qaidam Basin and its surrounding regions (Part 1): The southern Qilian Shan–Nan Shan thrust belt and northern Qaidam Basin: Geological Society of America Bulletin, v. 120, no. 7–8, p. 813–846, doi:10.1130/B26180.1.

Yin, A., Dang, Y.Q., Zhang, M., Chen, X.H., and McRivette, M.W., 2008b, Cenozoic tectonic evolution of the Qaidam Basin and its surrounding regions (Part 3): Structural geology, sedimentation, and regional tectonic reconstruction: Geological Society of America Bulletin, v. 120, no. 7–8, p. 847–876, doi:10.1130/B26232.1.

Yuan, D.Y., Zhang, P.Z., Lei, Z.S., Liu, B.C., and Liu, X.L., 2005, A preliminary study on the new activity features of the Lajishan mountain fault zone in Qinghai province: Earthquake Research in China, v. 19, no. 4, p. 391–401.

Zhai, Y., and Cai, T., 1984, The Tertiary system of Gansu Province, Wang, Y.M., ed., *in* Gansu Geology: Lanzhou, China, People's Press of Gansu, p. 1–40 (in Chinese).

Zhang, H.P., Craddock, W.H., Lease, R.O., Wang, W.T., Yuan, D.Y., Zhang, P.Z., Molnar, P., Zheng, D.W., and Zheng, W.J., 2011, Magnetostratigraphy of the Neogene Chaka Basin and its implications for mountain building processes in the north-eastern Tibetan Plateau: Basin Research (in press), doi:10.1111/j.1365-2117.2011.00512.x.

Zheng, D.W., Zhang, P.Z., Wan, J.L., Li, C., and Cao, J., 2003, Late Cenozoic deformation subsequence in northeastern Tibet: Detrital AFT records from Linxia Basin: Science in China, v. 46, p. 266–275.

Zheng, D.W., Zhang, P.Z., Wan, J.L., Yuan, D.Y., Li, C.Y., Yin, G.M., Zhang, G.L., Wang, Z.C., Min, W., and Chen, J., 2006, Rapid exhumation at ~8 Ma on the Liupan Shan thrust fault from apatite fission-track thermochronology: Implications for growth of the northeastern Tibetan Plateau margin: Earth and Planetary Science Letters, v. 248, no. 1–2, p. 198–208, doi:10.1016/j.epsl.2006.05.023.

Zheng, D.W., Clark, M.K., Zhang, P.Z., Zheng, W., and Farley, K.A., 2010, Erosion, fault initiation and topographic growth of the North Qilian Shan (northern Tibetan Plateau): Geosphere, v. 6, no. 6, p. 1–5, doi:10.1130/GES00523.1.